Advance Access publication 2023 June 8

# Radio variable and transient sources on minute time-scales in the ASKAP pilot surveys

Yuanming Wang (王远明) <sup>⑤</sup>, <sup>1,2,3</sup>★ Tara Murphy <sup>⑥</sup>, <sup>1,3</sup>★ Emil Lenc <sup>⑥</sup>, <sup>2</sup> Louis Mercorelli, <sup>4</sup> Laura Driessen <sup>6</sup>, <sup>1,5</sup> Joshua Pritchard <sup>6</sup>, <sup>1,2,3</sup> Baoqiang Lao (劳保强), <sup>6,7</sup> David L. Kaplan <sup>6</sup>, <sup>8</sup> Tao An (安 涛)<sup>5</sup>, Keith W. Bannister, George Heald 5, Shuoying Lu (卢铄迎), Artem Tuntsov, Mark Walker Walker and Andrew Zic <sup>102</sup>

Accepted 2023 June 2. Received 2023 May 16; in original form 2023 February 9

#### **ABSTRACT**

We present results from a radio survey for variable and transient sources on 15-min time-scales, using the Australian SKA Pathfinder (ASKAP) pilot surveys. The pilot surveys consist of 505 h of observations conducted at around 1 GHz observing frequency, with a total sky coverage of  $1476 \, \text{deg}^2$ . Each observation was tracked for approximately  $8 - 10 \, \text{h}$ , with a typical rms sensitivity of  $\sim 30 \,\mu$ Jy beam<sup>-1</sup> and an angular resolution of  $\sim 12$  arcsec. The variability search was conducted within each  $8-10 \,\mathrm{h}$ observation on a 15-min time-scale. We detected 38 variable and transient sources. Seven of them are known pulsars, including an eclipsing millisecond pulsar, PSR J2039-5617. Another eight sources are stars, only one of which has been previously identified as a radio star. For the remaining 23 objects, 22 are associated with active galactic nuclei or galaxies (including the five intra-hour variables that have been reported previously), and their variations are caused by discrete, local plasma screens. The remaining source has no multiwavelength counterparts and is therefore yet to be identified. This is the first large-scale radio survey for variables and transient sources on minute time-scales at a sub-mJy sensitivity level. We expect to discover ~1 highly variable source per day using the same technique on the full ASKAP surveys.

Key words: radio continuum: transients – radio continuum: stars – pulsars: general – stars: low-mass.

# 1 INTRODUCTION

Radio variable and transient sources usually imply extreme astrophysical environments including (intrinsic) strong magnetic activities, explosions, accretion, and (extrinsic) propagation effects caused by inhomogeneities in the ionized interstellar medium (ISM) (e.g. see Cordes, Lazio & McLaughlin 2004; Murphy et al. 2013). Early untargeted surveys for radio variables have led to a few discoveries (e.g. Levinson et al. 2002; Hyman et al. 2005; Gal-Yam et al. 2006). However, these surveys are historically limited by narrow fields of view (FoV), poor sensitivity, or sparse observing cadence (e.g. Bower et al. 2007; Bannister et al. 2011; Bell et al. 2011). Recently-built or upgraded telescopes have significant improvements, allowing for large-scale radio transient surveys with greatly increased sensitivity,

\* E-mail: ywan3191@uni.sydney.edu.au (YW); tara.murphy@sydney.edu.au

such as the Variables and Slow Transients (VAST) survey using the Australian SKA Pathfinder (ASKAP; Hotan et al. 2021) at 0.7 - 1.8 GHz (Murphy et al. 2013, 2021); the ThunderKAT imageplane transients programme using MeerKAT at ~GHz (Fender et al. 2016); the Murchison Widefield Array Transients Survey at 154 MHz (Bell et al. 2019); and the Amsterdam-ASTRON Radio Transients Facility and Analysis Center (AARTFAAC) all-sky monitor using the Low Frequency Array (LOFAR) at 10 – 90 MHz (Prasad et al. 2016). Other large-scale radio continuum surveys such as the TIFR Giant Metrewave Radio Telescope Sky Survey (TGSS; Intema et al. 2017), the LOFAR Two-meter Sky Survey (LoTSS Shimwell et al. 2017), the Very Large Array (VLA) Sky Survey (VLASS; Lacy et al. 2020), the GaLactic, and Extragalactic All-sky Murchison Widefield Array (MWA) survey eXtended (GLEAM-X; Hurley-Walker et al. 2022a) can also be used for transients searches. These new-generation telescopes give great opportunities to explore the parameter space that was poorly-explored before, for example, short-

© 2023 The Author(s).

Published by Oxford University Press on behalf of Royal Astronomical Society. This is an Open Access article distributed under the terms of the Creative Commons Attribution License (http://creativecommons.org/licenses/by/4.0/), which permits unrestricted reuse, distribution, and reproduction in any medium, provided the original work is properly cited.

<sup>&</sup>lt;sup>1</sup>Sydney Institute for Astronomy, School of Physics, University of Sydney, Sydney, NSW 2006, Australia

<sup>&</sup>lt;sup>2</sup>Australia Telescope National Facility, CSIRO, Space and Astronomy, PO Box 76, Epping, NSW 1710, Australia

<sup>&</sup>lt;sup>3</sup>ARC Centre of Excellence for Gravitational Wave Discovery (OzGrav), PO Box 218, Hawthorn, VIC 3122, Australia

<sup>&</sup>lt;sup>4</sup>Sydney Informatics Hub, The University of Sydney, NSW 2006, Australia

<sup>&</sup>lt;sup>5</sup>Australia Telescope National Facility, CSIRO, Space and Astronomy, PO Box 1130, Bentley WA 6102, Australia

<sup>&</sup>lt;sup>6</sup>School of Physics and Astronomy, Yunnan University, Kunming 650091, China

<sup>&</sup>lt;sup>7</sup> Shanghai Astronomical Observatory, Key Laboratory of Radio Astronomy, Chinese Academy of Sciences, Shanghai 200030, China

<sup>&</sup>lt;sup>8</sup>Center for Gravitation, Cosmology, and Astrophysics, Department of Physics, University of Wisconsin-Milwaukee, PO Box 413, Milwaukee, WI 53201, USA

<sup>&</sup>lt;sup>9</sup>School of Information and Communication, Guilin University of Electronic Technology, Guilin 541004, China

<sup>&</sup>lt;sup>10</sup>Manly Astrophysics, 15/41–42 East Esplanade, Manly 2095, Australia

time-scale radio transients ( $\lesssim$ hours). Compared to previous surveys which usually performed on time-scales  $\gtrsim$ 1 d, transient and variable sources on shorter time-scales  $\sim$ minutes would be considerably different, mainly including flaring stars to pulsars, or external effects such as enhanced scintillation.

A wide range of stellar objects can emit highly circularly polarized radio flares on time-scales of ~minutes (see a review from Güdel 2002). These flares are most likely generated from coherent emission process, for example, plasma emission or electron cyclotron maser (ECM) emission, allowing constraints on the stellar magnetosphere through measured electron density (plasma emission) or magnetic field strength (ECM emission; see reviews from Dulk 1985 and Osten 2008). A recent ASKAP large-scale untargeted survey identified more than 30 radio flaring stars, and 23 of them have no previous radio detections (Pritchard et al. 2021). These stars have a broad range from M-dwarfs to magnetically chemically peculiar B-type stars, showing that wide-field surveys are efficient to discover previously unknown radio flaring stellar objects.

Pulsars are rapidly rotating neutron stars with beamed radio (and/or high-energy) emission from their magnetic poles (periods from milliseconds to seconds). The discovery of pulsars opened a new research field that allow to study neutron star physics, general relativity, and the interstellar medium (see Lorimer & Kramer 2012). Their radio emission is thought to be coherent and the emission mechanisms are not fully understood yet (see a review from Philippov & Kramer 2022). The variability of pulsars on ~minutes time-scales can be from a range of different origins, including deep nulling (pulse energy suddenly drops to zero and then suddenly returns back to its normal state; e.g. Backer 1970), eclipses in a binary system (e.g. Camilo et al. 2000), and diffractive scintillation (e.g. Narayan 1992). It is possible to discover new pulsars from radio continuum surveys based on their variability, polarization, and multiwavelength properties (e.g. Kaplan et al. 2019; Sobey et al. 2022; Wang et al. 2022).

Intra-hour variables (IHVs) are extreme scintillating active galactic nuclei (AGN) with large amplitude modulations ( $\gtrsim$ 10 per cent) and short time-scales ( $\lesssim$  hours), caused by small-scale irregularities in the ionized ISM with required pressure fluctuations much higher than those in the typical diffuse ISM (e.g. Kedziora-Chudczer et al. 1997; Dennett-Thorpe & de Bruyn 2002; Walker et al. 2017; Bignall et al. 2019; Oosterloo et al. 2020). There are studies showing that these high-pressure clouds are close to the Earth (a few parsecs) and their physical nature is still unclear (e.g. Dennett-Thorpe & de Bruyn 2003; Wang et al. 2021). IHV provides an opportunity to explore the possible origin of discrete plasma in the solar neighbourhood, as well as small-scale AGN strucutre.

More recently, there have been discoveries of ultra-long period neutron stars (e.g. Caleb et al. 2022; Hurley-Walker et al. 2022b). Their periods are unusually slow (18.18 min and 76 s) located beyond the 'death line' as defined by the inner vacuum-gap curvature radiation models for radio emission (Chen & Ruderman 1993), challenging our understanding of how these systems evolve. These discoveries highlighted the possibility of identifying new populations on these poorly-explored short time-scales.

Only a few radio transient surveys have covered the time-scales of ~minutes and resulted in a few (or no) convincing transients. Early surveys on minute-time-scales were mainly at low frequencies (tens of MHz) with low angular resolution (~degs) and poor sensitivity

(e.g. Lazio et al. 2010; Obenberger et al. 2014). The first survey explored minutes-time-scales at GHz is by Thyagarajan et al. (2011). They conducted an analysis for variable and transient radio sources down to ~mJy levels over time-scales from a few minutes to years using overlapped adjacent snapshot images (~3-min interval) of the Faint Images of the Radio Sky at Twenty-cm (FIRST) survey (Becker, White & Helfand 1995) at 1.4 GHz. They found several stars and pulsars accompanied with a large sample of unclassified or unidentified objects due to lack of multiwavelength identification. Stewart et al. (2016) searched for low-frequency transients on timescales of 0.5 - 297 min using LOFAR at a sensitivity of  $\sim$ Jy level. They found one transient with a duration of a few minutes and a flux density of 15 - 25 Jy at 60 MHz. The nature of this transient is still unclear. Hobbs et al. (2016) ran transient detection on 2min snapshot images from 13 h ASKAP-BETA observation for an intermittent pulsar PSR J1107 - 5907. They detected the target pulsar but no other transient events. Chiti et al. (2016) performed a search for radio transients on time-scales from seconds to minutes using more than 200 h VLA archival data at 5 and 8.4 GHz in the Galactic centre, with a typical detection threshold of  $\sim 100$  mJy. They detected two promising, unclassified candidates and suggested them as either a new astrophysical source or a subtle imaging artefact.

The key to achieve a transient survey on short-time-scales is a telescope with high instrumental sensitivity, large FoV, and more importantly, great instantaneous (u, v) coverage to build a good-quality sky model on a short sampling time. ASKAP is a survey instrument designed using phased array feed (PAF) technology (DeBoer et al. 2009; Hotan et al. 2021), which provides 36 beams for each of 36 12-m antennas to achieve a wide FoV and good sensitivity. The array configuration provides excellent instantaneous (u, v) coverage.  $^2$ , making snapshot imaging surveys (e.g. at 15-min time-scale) possible. With the ASKAP telescope we are now able to discover short-time-scale transients (seconds to hours) in a more systematic way. The improved large-scale multiwavelength surveys can also provide valuable information to identify detected transients.

In this paper we describe the first large-scale survey for radio variable and transient sources on a time-scale of 15 min using ASKAP pilot survey data. The data we used are from a large set of pilot survey projects, total of 505 h covering a total of 1476 deg² sky area at a sub-mJy sensitivity. In Section 2 we describe the survey data and processing process, with the following variability search described in Section 3. In Section 4 we present results from the survey and summarize properties of our candidates, and in Section 5 we discuss our sources, the variability rate, and the application of this approach to future surveys.

## 2 OBSERVATIONS AND DATA PROCESSING

ASKAP began its pilot survey program on 2019 July 15 (see Hotan et al. 2021, Section 15). This involved 11 continuum and spectral-line surveys, resulting in more than 1000 h of observations. The pilot surveys used their requested configurations and parameters, providing a rich archival data base<sup>3</sup> suitable for various science goals.

<sup>&</sup>lt;sup>1</sup>See a summary table in Mooley et al. (2016) and http://www.tauceti.caltec h.edu/kunal/radio-transient-surveys/index.html

<sup>&</sup>lt;sup>2</sup>https://www.atnf.csiro.au/projects/askap/newdocs/configs-3.pdf

<sup>&</sup>lt;sup>3</sup>All of the ASKAP data can be accessed through the CSIRO ASKAP Science Data Archive (CASDA) https://research.csiro.au/casda/

#### 2.1 Observations

We used ASKAP pilot survey data. Our aim was to search for intraobservation transients on 15-min time-scales in the image plane. We selected long observations (>1 h) that used the standard correlator mode (i.e. not the zoom mode) and no interleaving. Fig. 1 shows the total sky coverage of selected survey data. We mainly used observations from the following surveys

- (i) **EMU**: the Evolutionary Map of the Universe (EMU; project code AS101) aims to make a deep radio continuum all-sky map from declination of  $-90^{\circ}$  to  $+30^{\circ}$  and expects to detect and catalogue about 70 million galaxies (Norris et al. 2011). The EMU pilot survey was observed at a central frequency of 943.5 MHz with a bandwidth of 288 MHz. The integration time for each field is 10 h, reaching a sensitivity of 25 30  $\mu$ Jy beam<sup>-1</sup>at a spatial resolution of 11 18 arcsec (Norris et al. 2021). The sky area of the EMU pilot survey was within the Dark Energy Survey (DES; Abbott et al. 2018) field, which is helpful to identify any optical counterpart for a detected radio source.
- (ii) WALLABY: the Widefield ASKAP L-band Legacy All-sky Blind surveY (WALLABY; project code AS102) is a next-generation survey of neutral hydrogen (HI) in the Local Universe (Koribalski et al. 2020). The ASKAP pilot survey for WALLABY was conducted at a central frequency of 1367.5 MHz with a bandwidth of 144 MHz, targeting the Hydra cluster, the NGC 4636 group, and the Norma cluster. The integration time for each observation was 8 h. WALLABY used a different beam configuration, square\_6x6 (a square grid arrangement), compared to other surveys such as EMU. The latter normally used closepack36 arrangement (see Fig. 2), which offsets alternating rows for a more uniform sensitivity (see Section 9 in Hotan et al. 2021).
- (iii) **POSSUM**: the Polarization Sky Survey of the Universe's Magnetism (POSSUM; project code AS103) aims to measure the Faraday rotation of three million extragalactic radio sources over 30 000 square degrees, improving the understanding of astrophysical magnetism (Gaensler et al. 2010). The ASKAP pilot survey for POSSUM targeted to same sky region with EMU, tracked for 8 h but at a higher central frequency of 1367.5 MHz with a bandwidth of 144 MHz.
- (iv) **ASKAP GW**: the ASKAP Follow-up Observations for Gravitational Wave Counterparts (ASKAP GW; project code AS111) aimed to conduct searches for radio afterglows of gravitational wave events GW190814 (Dobie et al. 2019, 2022). It contains 10 observations separated by days to months. The integration time for each observation is approximately 10.5 h, achieving a sensitivity of 35–40  $\mu$ Jy beam<sup>-1</sup>at a spatial resolution of 12  $\times$  10 arcsec (Dobie et al. 2022). The first four epochs (SB9602, 9649, 9910, and 10463) were used by Wang et al. (2021) to demonstrate intra-observation transients searches with ASKAP, resulting in the discovery of a long, thin, and straight plasma filament revealed by five IHVs in a line on the sky.
- (v) **SWAG-X**: the GAMA-09 + X-ray survey (SWAG-X; project code AS112) was designed to cover the GAMA<sup>4</sup> and eROSITA<sup>5</sup> Final Equatorial-Depth Survey (Moss et al., in prep). SWAG-X tiles were located farther north than most other data, and were observed at a central frequency of 887.5 MHz with a bandwidth of 288 MHz.
- (vi) **Other ToOs**: we also included two observations from target of opportunity observations (ToOs) or guest observations (project

code AS113). The two ASKAP fields were scheduled to align with Sector 36 observed by the *Transiting Exoplanet Survey Satellite* (*TESS*; Ricker et al. 2015). The integration time for each field is 13 h, achieving a rms sensitivity of  $21-24 \,\mu\text{Jy} \,\text{beam}^{-1}$ at a central frequency of 887.5 MHz (see details in Rigney et al. 2022).

Table 1 lists details for 52 observations selected from the earlier surveys. Each observation was approximately  $8-10\,h$ , with a FoV up to  $66\,deg^2$  at the low-frequency band (887.5/943.5 MHz) and down to  $29\,deg^2$  at high-frequency band (1367.5 MHz). An example image (from one of EMU observations) is shown in Fig. 2, overlapped with a typical beam configuration closepack36 in  $0.9^\circ$  pitch<sup>6</sup> The total observing time was  $505\,h$  and the overall (unique) sky coverage reached  $1476\,deg^2$  (note POSSUM was overlapped with EMU), including an extremely deep field S190814bv with total tracking time of approximately  $115\,h$ .

## 2.2 Processing workflow

- Fig. 3 shows the overall data processing workflow, from raw visibilities, standard ASKAP outputs, to our final products. The processing consists of three parts performed at different sites: the standard ASKAP processing at the Pawsey Supercomputing Research Centre.<sup>7</sup> in Western Australia, our dedicated processing for transients search at the China SKA regional centre, and the final candidates inspection and investigation by VAST team on the local machine. Further, we give a description of each processing step.
- (i) **Raw data ingest**: raw visibility data from the ASKAP correlator hardware are automatically ingested to the Pawsey Supercomputing Research Centre. Each of the PAF beams were split into its own measurement set, that is, total of 36 measurement sets for one observation.
- (ii) ASKAP science data processing: each ASKAP observation was processed using the ASKAPSOFT pipeline (Guzman et al. 2019; Whiting 2020) following the standard procedure described in Hotan et al. (2021, Section 11). This includes bandpass calibration (using a separate observation of PKS B1934–638), radio-frequency interference (RFI) flagging, initial imaging and self-calibration, wide-field imaging (per beam), and linear mosaicking (to create a full-field image). After the mosaicked full-field images have been produced, source finding is run to create catalogues using SELAVY (Whiting & Humphreys 2012).
- (iii) **Deposit to CASDA**: the standard ASKAP data products, including calibrated visibilities at continuum resolution, mosaicked full-field images, and corresponding SELAVY catalogues, are deposited to CSIRO ASKAP Science Data Archive (CASDA<sup>8</sup>).

After the data have been uploaded to CASDA, we download the calibrated visibilities through the CASDA virtual observatory (VO) services<sup>9</sup> to the China SKA regional centre prototype (CSRC-P; An, Wu & Hong 2019; An et al. 2022) in Shanghai. The data transferring takes about 2 – 3 h for a 10 h observation. We then conduct our dedicated processing for transients search on 15-min time-scale. The CSRC-P is equipped with 23 multicore x86 CPU nodes with memory size of 0.77–1 TB each, allowing for the parallel processing of 36 beams from a single observation. Further is a description of each step,

<sup>&</sup>lt;sup>4</sup>http://www.gama-survey.org/

<sup>&</sup>lt;sup>5</sup>https://www.mpe.mpg.de/eROSITA

<sup>&</sup>lt;sup>6</sup>Pitch represents the spacing of neighbouring beam centre. See Fig. 2

<sup>&</sup>lt;sup>7</sup>https://pawsey.org.au/

<sup>8</sup>https://research.csiro.au/casda/

<sup>9</sup>https://casda.csiro.au/casda\_vo\_tools/tap

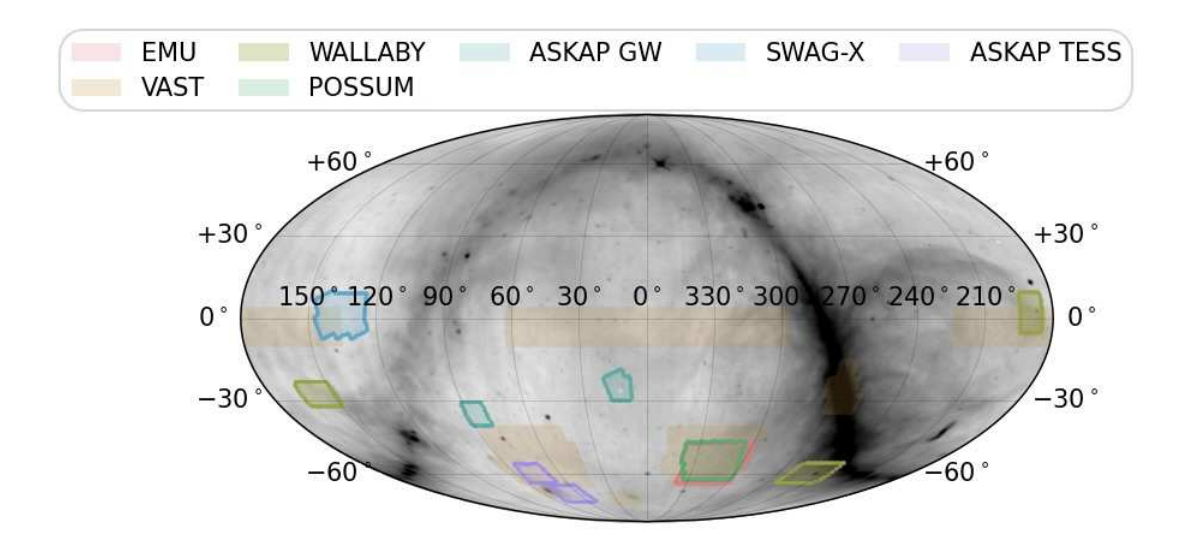
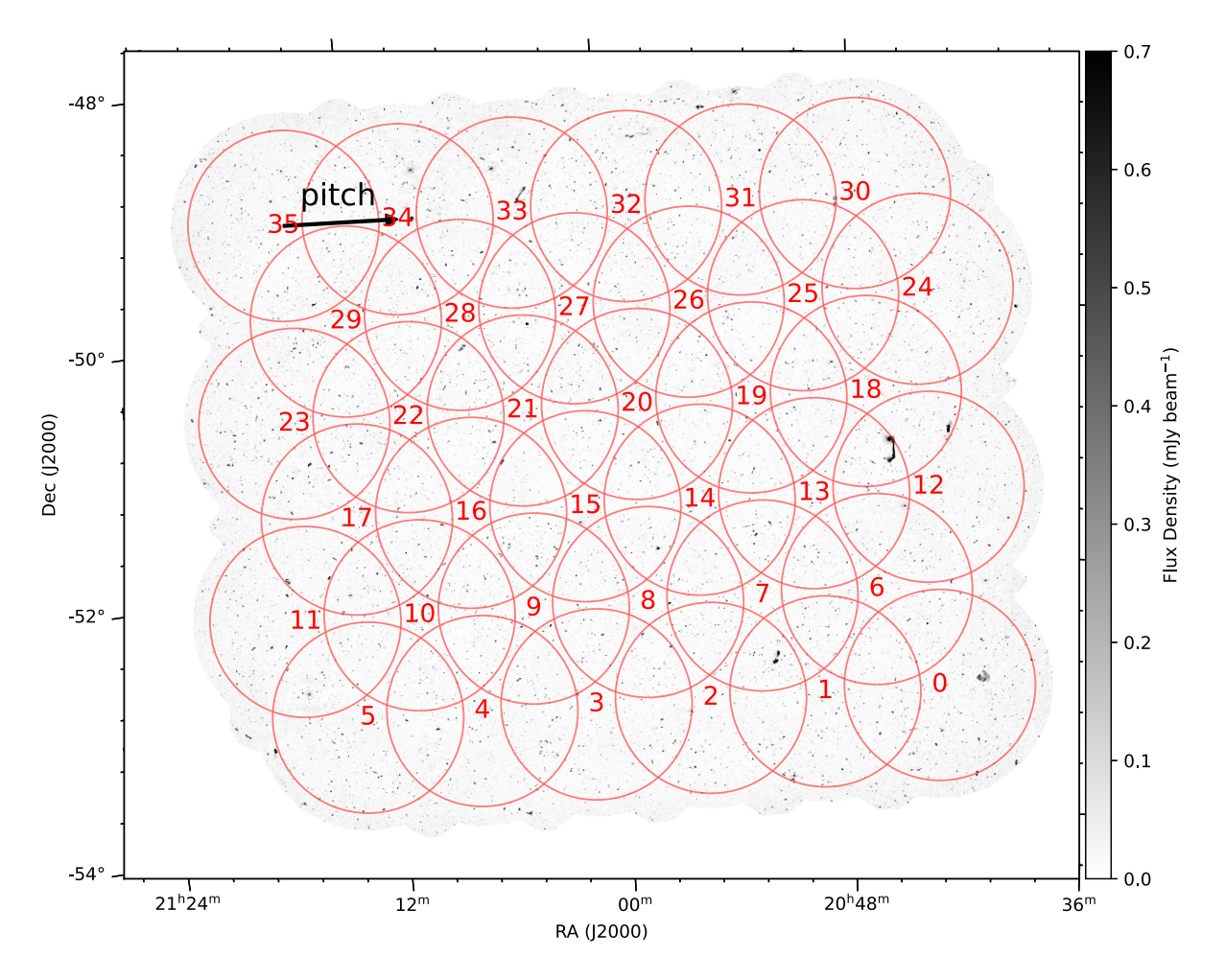


Figure 1. Sky coverage of ASKAP pilot survey data we used in this study. The sky map is plotted with J2000 equatorial coordinates in the Mollweide projection and the background diffuse Galactic emission at 887.5 MHz is modelled from Zheng et al. (2017).



**Figure 2.** An example ASKAP image from one of the EMU observations (SB9287). The red circles represent the arrangement of the 36 beams in the closepack36 configuration, numbered from 0 to 35. The pitch spacing is  $0.9^{\circ}$  and the actual full-width half maximum for the primary beam is approximately  $1.5^{\circ}$  at 943.5 MHz (as represented by the red circle). The background image is a mosaiced version made by combining the separate images for each beam. Note that we processed and analysed each beam independently across the whole paper.

**Table 1.** Details of the 52 ASKAP pilot observations we used in this work, including the scheduling block ID (SBID), field name, coordinates of field center in J2000, central frequency (unit of MHz), observing start time in UTC, and the duration of each observation. The SBID and project code can be used to access the data via the CSIRO ASKAP Science Data Archive.

SBID	Field name	RA (hh:mm:ss)	Dec. (dd:mm:ss)	Cent. freq. (MHz)	Star time (UTC)	Duration (hh:mm:ss)	Project code
9287	EMU_2059-51	21:00:30.210	-51:11:32.074	943.5	2019 July 15 13:49:08	10:00:11	AS101
9325	EMU_2034-60	20:35:13.283	-60:24:59.883	943.5	2019 July 17 13:23:37	10:00:11	AS101
9351	EMU_2042-55	20:42:40.597	-55:48:29.838	943.5	2019 July 18 13:35:59	10:00:11	AS101
9410	EMU_2115-60	21:16:21.856	-60:24:59.883	943.5	2019 July 24 12:23:45	10:00:11	AS101
9434	EMU_2132-51	21:33:13.847	-51:11:32.074	943.5	2019 July 25 13:16:38	10:00:11	AS101
9437	EMU_2027-51	20:27:46.574	-51:11:32.074	943.5	2019 July 26 11:26:23	10:00:11	AS101
9442	EMU_2118-55	21:18:40.597	-55:48:29.838	943.5	2019 July 27 12:13:06	10:00:11	AS101
9501	EMU_2156-60	21:57:30.427	-60:24:59.883	943.5	2019 Aug 02 12:28:01	10:00:01	AS101
10 083	EMU_2154-55	21:54:40.597	-55:48:29.838	943.5	2019 Oct 03 08:21:36	10:00:11	AS101
10 635	EMU_2205-51	22:05:57.482	-51:11:32.074	943.5	2019 Nov 24 06:10:19	10:00:11	AS101
10636	Abell_3266	04:32:25.107	-61:32:30.178	943.5	2019 Nov 24 16:11:40	6:45:05	AS101
10 269	Hydra_1B	10:17:51.611	-27:49:21.388	1367.5	2019 Oct 25 19:23:48	8:00:04	AS102
10 609	Hydra_1A	10:15:48.413	-27:22:48.299	1367.5	2019 Nov 20 18:33:48	8:00:14	AS102
10612	Hydra_2A	10:39:24.807	-27:22:48.299	1367.5	2019 Nov 21 18:52:37	8:00:04	AS102
10 626	Hydra_2B	10:41:28.005	-27:49:21.388	1367.5	2019 Nov 23 18:47:26	8:00:04	AS102
10736	NGC4636_2A	12:38:02.392	+04:57:09.446	1367.5	2019 Dec 05 19:56:50	8:37:24	AS102
10 809	NGC4636_1A	12:38:02.134	-00:26:53.976	1367.5	2019 Dec 12 19:28:22	8:39:03	AS102
10812	NGC4636_1B	12:39:50.199	-00:53:55.037	1367.5	2019 Dec 13 19:26:17	8:38:53	AS102
11 816	Norma_1A	16:16:35.826	-59:29:14.718	1367.5	2020 Feb 14 18:56:01	8:00:04	AS102
11 832	Norma_1B	16:20:16.779	-59:54:55.768	1367.5	2020 Feb 15 18:54:46	8:00:14	AS102
12 193	Norma_2A	16:55:30.959	-59:29:14.718	1367.5	2020 Mar 13 17:43:41	8:00:04	AS102
12 209	Norma_2B	16:59:11.914	-59:54:55.768	1367.5	2020 Mar 14 17:43:36	8:00:04	AS102
9945	POSSUM_pilot_2032-54	20:32:37.797	-54:37:17.255	1367.5	2019 Sep 19 10:03:21	9:34:08	AS103
9962	POSSUM_2045-50	20:46:04.907	-50:44:45.633	1367.5	2019 Sep 20 09:05:46	10:00:01	AS103
9972	POSSUM_2038-58	20:39:00.327	-58:26:20.890	1367.5	2019 Sep 21 09:12:02	10:00:11	AS103
9975	POSSUM_2057-54	20:57:37.797	-54:37:17.255	1367.5	2019 Sep 22 09:17:35	10:00:01	AS103
9983	POSSUM_2113-50	21:13:25.953	-50:47:31.669	1367.5	2019 Sep 23 09:21:06	10:00:11	AS103
9992	POSSUM_2110-58	21:11:16.872	-58:29:41.342	1367.5	2019 Sep 24 09:32:25	10:00:11	AS103
10 007	POSSUM_2126-54	21:27:15.485	-54:40:10.601	1367.5	2019 Sep 25 09:35:22	10:00:11	AS103
10 040	POSSUM_2156-54	21:56:55.161	-54:42:41.796	1367.5	2019 Sep 28 09:53:15	10:00:11	AS103
10 043	POSSUM_2207-50	22:08:12.569	-50:52:12.774	1367.5	2019 Sep 29 09:52:20	10:00:01	AS103
10 168	POSSUM_2140-50	21:40:48.566	-50:50:01.774	1367.5	2019 Oct 16 08:18:08	8:43:22	AS103
9596	LIGO_0556-3309	05:56:28.987	-33:11:53.141	943.5	2019 Aug 15 19:35:14	10:00:01	AS111
9602	S190814bv	00:50:43.726	-25:19:04.988	943.5	2019 Aug 16 14:11:23	10:38:10	AS111
9649	S190814bv	00:50:43.726	-25:19:04.988	943.5	2019 Aug 23 13:43:55	10:37:40	AS111
9910	S190814bv	00:50:43.726	-25:19:04.988	943.5	2019 Sep 16 12:09:33	10:37:20	AS111
10 463	S190814bv	00:50:43.726	-25:19:04.988	943.5	2019 Nov 07 08:45:10	10:37:20	AS111
12 704	S190814bv	00:50:43.726	-25:19:04.988	943.5	2020 Apr 03 23:00:00	34:32:46 <sup>a</sup>	AS111
13 570	S190814bv	00:58:07.108	-23:44:33.168	943.5	2020 Apr 29 21:41:11	10:00:11	$AS107^b$
15 191	S190814bv	00:50:43.726	-25:19:04.988	943.5	2020 July 03 17:01:21	10:30:12	AS111
18 912	S190814bv	00:50:43.726	-25:19:04.988	943.5	2020 Nov 29 07:15:32	10:52:26 <sup>a</sup>	AS111
18 925	S190814bv	00:50:43.726	-25:19:04.988	943.5	2020 Nov 28 09:18:30	8:53:19	AS111
27 379	S190814bv	00:50:37.426	-25:17:00.371	943.5	2021 May 29 19:23:45	10:30:12	AS111
10 108	eFEDS_low_T1-1A	09:03:59.506	+04:39:12.756	887.5	2019 Oct 05 20:09:37	8:38:53	AS112
10 123	eFEDS_low_T0-1A	08:38:44.323	+04:38:40.490	887.5	2019 Oct 07 19:47:17	8:41:23	AS112
10 126	eFEDS_low_T0-0A	08:38:49.891	-01:39:23.893	887.5	2019 Oct 08 19:36:54	8:38:53	AS112
10 129	eFEDS_low_T1-0A	09:03:59.635	-01:38:52.067	887.5	2019 Oct 09 20:24:35	7:32:22	AS112
10 132	eFEDS_low_T2-1A	09:29:15.225	+04:38:28.707	887.5	2019 Oct 10 20:27:09	8:39:03	AS112
10 135	eFEDS_low_T2-0A	09:29:09.378	-01:39:24.359	887.5	2019 Oct 10 20:27:03 2019 Oct 11 20:29:23	8:33:45	AS112
10 137	eFEDS_low_T1-0A	09:03:59.635	-01:38:52.067	887.5	2019 Oct 12 19:51:28	8:39:03	AS112
25 035	TESS_Sector-36A	04:24:00.754	-70:02:20.506	887.5	2021 Mar 20 03:05:00	13:00:00	AS113
	TESS_Sector-36B	05:08:01.681	-60:01:10.217	887.5	2021 Mar 21 03:31:14	12:57:11	AS113

*Notes.* <sup>a</sup> These data sets consist of two observations with  $\gtrsim$  hours-long gap between them. The overall integration time is 15.3 h for SB12704 and 7.1 h for SB18912. See details in Dobie et al. (2022)

including estimated processing time for a typical 10 h observation (in brackets).

(i) **Model creation** (15 - 20h): the sky model is created using calibrated visibility data. See description in Section 2.3.1.

<sup>&</sup>lt;sup>b</sup> This is a test observation to rule out potential instrumental effects, as described in Wang et al. (2021). This observation is under a different project code AS107 (the ASKAP Variables and Slow Transients; VAST; Murphy et al. 2013)

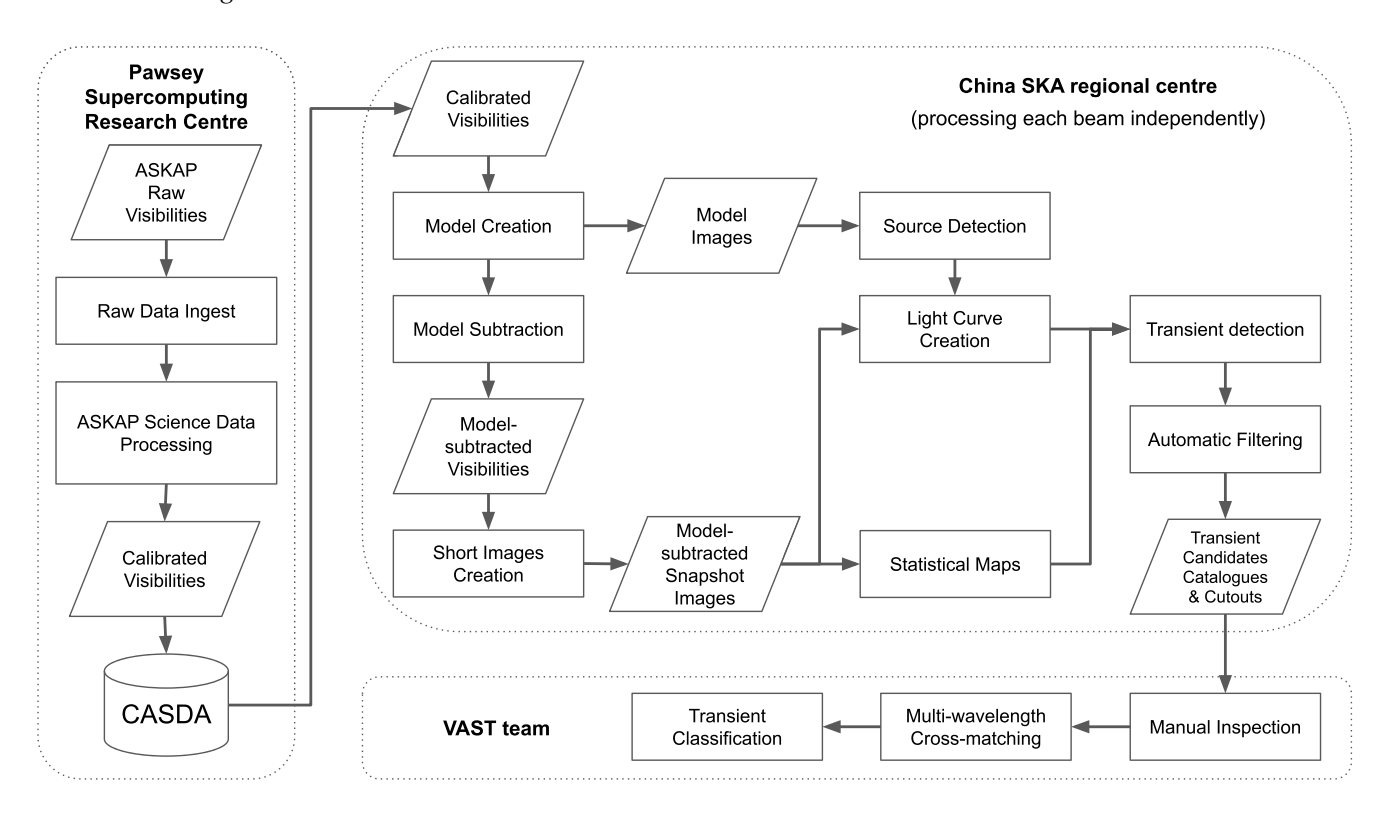


Figure 3. Illustration of the data processing workflow. A description of each stage is given in Section 2.2.

- (ii) **Model subtraction** (*a few minutes*): the model visibilities are subtracted from the original calibrated visibilities.
- (iii) Short image creation (1 h): a series of model-subtracted snapshot images (15-min time-step in this work) are generated using the model-subtracted visibilities. See description in Section 2.3.2.
- (iv) **Source detection** (*a few minutes*): untargeted source finding is run on model images. See description in Section 3.
- (v) **Light-curve creation** (<1 min): for each source detected in model images, a radio light curve is formed by collecting flux measurements from all model-subtracted snapshot images. See description in Section 3.1.
- (vi) **Statistical map analysis** ( $10 30 \, min$ ): the model-subtracted snapshot images are used to form several statistical maps for further variability analysis. See description in Section 3.2.
- (vii) **Transient detection** (<*1 min*): the generated light curves and statistical maps are analysed to detect transient or variable behaviour. See detection criteria in Section 3.
- (viii) **Automatic Filtering** (<1 min): candidates that meet metrics listed in Section 3.1 are automatically discarded.

The final data products are candidates catalogues, and model image cutouts, animations made from model-subtracted snapshot images for each transient candidate. These final products are transferred to the VAST local machine for manual inspection and further investigation, described as follows:

- (i) **Manual inspection**: the candidates are manually inspected to confirm if they are real transients.
- (ii) **Multiwavelength cross-matching**: sources that exhibit transient or variable behaviour are cross-matched with multiwavelength catalogues to investigate their nature. See details in Section 4.
- (iii) Transient classification: sources that exhibit transient or variable behaviour are classified based on their multiwavelength

information and/or other follow-up observations. See details in Section  $\mathbf{4}$ 

In summary, the overall processing time for a  $10\,h$  observation (36 beams in parallel) is about  $1-2\,d$  to get final transient candidates. The processing time is mainly limited by the model creation process. We discuss possible ways to improve this in Section 5.5. A detailed description of our dedicated data processing parameters is given in Section 2.3.

#### 2.3 Processing parameters

Each observation was calibrated and processed following the standard procedure (see detailed description in each survey paper, e.g. Dobie et al. 2019; Koribalski et al. 2020; Norris et al. 2021). After calibration, flagging, and self-calibration, the processed visibilities for each observation (total of 36 visibility sets, one for each of 36 beams) were uploaded to CASDA. These calibrated visibilities were used for our dedicated processing described as further. We processed each beam independently.

## 2.3.1 Model images

We reduced the data using the Common Astronomy Software Applications package (CASA; McMullin et al. 2007). For individual beams we created independent model images using CASA tclean task from the self-calibrated visibilities. We used multiscale multifrequency synthesis with two Taylor terms (Rau & Cornwell 2011) to allow modelling the spectral curvature during the deconvolution process to obtain a better model at the reference frequency. We performed a deep clean with 10 000 iterations using Briggs weighting (robustness of 0.5) to obtain a good balance between resolution and sensitivity (Briggs 1995). We chose an image cell size of 2.5 arcsec and a

large image size of  $10\,000\times10\,000$  pixels to include as many of neighbouring (bright) sources into the model, reducing side-lobes effects. The typical residual rms is about  $50\,\mu\mathrm{Jy}$  beam $^{-1}$  for observations at low-frequency band and  $35\,\mu\mathrm{Jy}$  beam $^{-1}$  for observations at mid-frequency band. Future improvements would include flexible pixel size settings (for observation at different frequencies) and better handling of nearby bright sources (e.g. 'A' sources peeling). For each observation we obtained 36 separate model images.

#### 2.3.2 Model-subtracted snapshot images

We converted each model image to model visibilities, and subtracted the model visibilities from the original self-calibrated visibilities. We imaged the resulting model-subtracted visibilities in 15-min timesteps using the same weighting parameters as earlier. We chose a square image size of 3000 pixels ( $\sim$ 2.1°), which is approximately 1.5 times the primary beam diameter at 943.5 MHz. We did not apply any deconvolution during this step as the model has already been subtracted from the calibrated visibilities. We did not perform any primary beam effect correction either as we were only interested in the relative flux densities of source variations along with time. For a typical 10 h observation, we generated 40 model-subtracted snapshot images for each beam. The median rms noise for each model-subtracted snapshot image is about 200  $\mu$ Jy beam $^{-1}$ .

# 3 VARIABILITY SEARCH

We conducted a variability search using the model-subtracted 15-min snapshot images. Our search contains two different analysis methods. First, we did light-curve analysis focusing on characterizing light curves of all sources detected in the deep model images. Secondly, we did image analysis focusing on producing statistical maps (e.g. chi-square map and peak map) using all model-subtracted snapshot images and selecting any candidates that stood out in the map. The image analysis used a slightly stricter threshold to select candidates compared to the light-curve analysis as we do not use prior information of source positions in the searching process, but the advantage is being able to find any extreme transients (e.g. a single flare) that were not detected in the model images. We describe each of these approaches further.

For both methods a source catalogue from the model image was necessary as a reference to rule out false candidates. We used AEGEAN (Hancock et al. 2012; Hancock, Trott & Hurley-Walker 2018) to perform source finding at a  $6\sigma$  threshold in model images and the built-in package BANE to estimate the background and rms noise levels. We detected approximately 1000 sources in each model image (per beam). Note that the model image size is about  $2.1 \times 2.1 \text{ deg}^2$  and therefore there is an overlap for model images of neighbouring beams (beam spacing is  $0.9^\circ$ ), which means most of sources are detected at least twice in neighbouring model images – this is useful for checking the reliability of any measured variations.

#### 3.1 Light-curve analysis

For each source detected in the model image of a given beam, we converted the global coordinate to the pixel position in each image, and extracted its light curve as follows

- (i) measured the flux density in the deep restored model image  $S_{\text{deep}}$  at the given pixel position;
- (ii) measured the flux density on the *i*-th snapshot images  $S_{i, \text{snap}}$  at given pixel position;

- (iii) measured the residual flux density  $S_{residual}$  on the sky model residual image; and
  - (iv) the *i*-th data point of the light curve is then given by

$$S_i = S_{\text{deep}} + S_{i,\text{snap}} - S_{\text{residual}} \tag{1}$$

For each light curve, we calculated the weighted reduced  $\chi^2$  (defined as  $\eta$ ) to measure the significance of random variability using

$$\eta = \frac{1}{N-1} \sum_{i=1}^{n} \frac{\left(S_i - \bar{S}\right)^2}{\sigma_i^2},\tag{2}$$

where N is the total number of measurements in the light curve (i.e. the number of model-subtracted snapshot images),  $\sigma_i$  is the local rms measured at i-th snapshot image using BANE, and  $\bar{S}$  is the weighted mean flux density defined as

$$\bar{S} = \frac{\sum_{i=1}^{n} \left( S_i / \sigma_i^2 \right)}{\sum_{i=1}^{n} \left( 1 / \sigma_i^2 \right)} \tag{3}$$

As discussed in Rowlinson et al. (2019), the histogram of  $\eta$  for all sources follows an approximately Gaussian distribution in logarithmic space. Since all stable sources will follow this distribution, any sources with excessively large  $\eta$  are considered to be variable sources. In this paper we selected candidates with  $\eta > 2.0\sigma_{\eta}$  where  $\sigma_{\eta}$  is the standard deviation measured by fitting a Gaussian function to the  $\eta$  distribution.

We also calculated the weighted modulation index to measure the magnitude of variability using

$$m = \frac{\sigma_{\rm s}}{\bar{\rm s}},\tag{4}$$

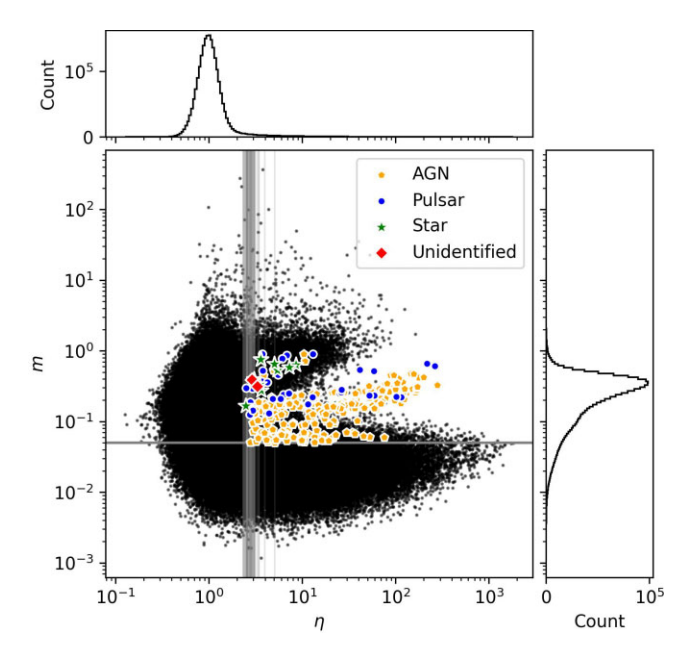
where  $\sigma_s$  is the standard deviation of flux densities of the light curve. We considered any candidates with  $m \leq 5$  per cent as non-variable. We ruled out extended sources (using the integrated-to-peak criterion further) as the varying (u, v) coverage during the observation can result in the measured flux density varying in different parts of the extended source. We also ruled out candidates near the edge of the beam.

Fig. 4 shows the distribution of sources in the variability metrics  $\eta$  and m, defined in equations (2) and (4). The  $2\sigma_{\eta}$  threshold corresponds to  $\eta \sim 2.5-3.0$  for the majority of fields. We noticed that objects in SB11832 has excessively large variability metrics compared to other fields (e.g. with a median  $\eta \sim 2.5$  and  $2\sigma_{\eta} \sim 11$ ). After investigation this field contains a Jy-level source PKS 1613-586, and its side-lobes largely affect many beams in this field. We discarded SB11832 in the following analysis.

In summary, we selected candidates based on the following metrics:

- (i)  $\eta > 2.0\sigma_{\eta}$  where  $\sigma_{\eta}$  is measured from the  $\eta$  distribution for all sources in each beam;
  - (ii) m > 0.05;
  - (iii) ratio of integrated to peak flux density <1.5;
- (iv) located within about one full-width half maximum (FWHM) from the beam centre, that is, <0.8 deg for observations at 887.5 MHz and 943.5 MHz and <0.6 deg for observations at 1367.5 MHz.

All candidates that passed the above metrics were subject to further manual inspection to rule out artefacts near bright sources and/or caused by rotated (u.v) sampling. We identified a total of 35 unique variable sources (as shown in the top-right quadrant of Fig. 4). We compared the light curve of each source with that in neighbouring beams to confirm that the variability is genuine.



**Figure 4.** Distribution of the two key variability metrics,  $\eta$  and m, for all sources in the light-curve analysis. The grey lines represent the selection thresholds (i.e. m > 0.05 and  $\eta > 2.0\sigma_{\eta}$ ). The thresholds for  $\eta$  is around 2.5 – 3.0 for the majority of fields. The colourful markers represent classified variable and transient sources: AGNs (orange pentagons), pulsars (purple circles), stars (green stars), and unidentified objects (red diamonds). See details in Section 4. Each unique source corresponds to multiple light-curves detections from neighbouring beams and/or overlapped fields. Another population of detections above the threshold (at  $m \sim 1$ ) are mostly false candidates near bright sources.

## 3.2 Statistical map analysis

The light-curve approach is sensitive to all variable sources detected in the model images. However, it cannot identify transient events that were not detected in an hours-long model image (e.g. single flare events; see an example in Fig. 5).

Hence we used a different approach generating different statistical maps (e.g. chi-square map, peak map, and Gaussian map) made from model-subtracted snapshot images, in order to identify transient phenomena independent of whether they were detected in model images. We first generated a cube for each beam using a series of model-subtracted snapshot images. For a 10-h observation, the resulting cube size in pixel is [40 3000 3000]. The first axis is time (a total of 40 15-min images for a 10-h observation), and the other two axes are the spatial dimensions (a size of 3000 pixels on each dimension). For each spatial pixel  $(x_p, y_p)$  we extracted its flux density in *i*-th snapshot image to form a light-curve series  $S(x_p, y_p)$ . We generated 2D statistical maps using measured  $S(x_p, y_p)$  as discussed further.

- (i) **Chi-square map:** we calculated the weighted reduced chi-square at each spatial pixel  $\eta(x_p, y_p)$  based on extracted  $S(x_p, y_p)$  using equation (2). The chi-square map is therefore made up of  $3000 \times 3000$  measured  $\eta(x_p, y_p)$  values. For pixels with no, or weak, variability along the time axis, the resulting  $\eta(x_p, y_p)$  should be around 1. As defined in equation (2), the chi-square map is sensitive to any random variability, but less sensitive to a single flare event.
- (ii) **Peak map**: the peak map is the peak value measured in the time series for each  $(x_p, y_p)$ . Instead of using the measured flux density  $S(x_p, y_p)$  directly, we calculated the signal-to-noise ratio SNR =  $S_{i, \text{snap}}/\sigma_i$  at each  $(x_p, y_p)$ . We selected the peak SNR $(x_p, y_p)$  along

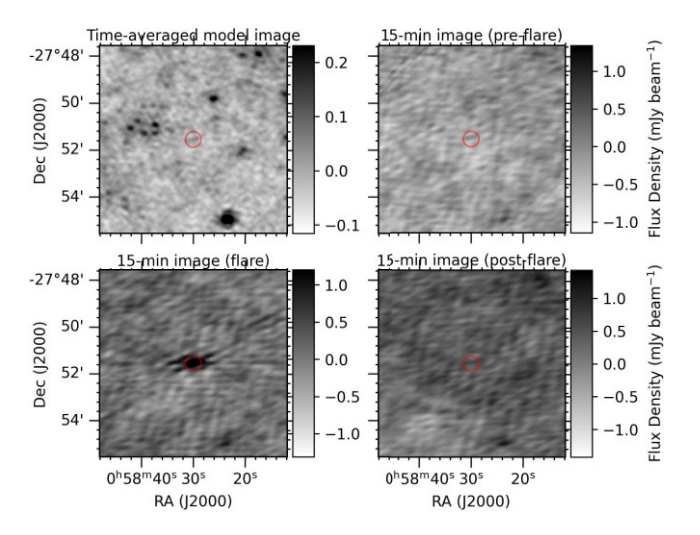


**Figure 5.** Time-averaged model image (top left) and 15-min model-subtracted snapshot images before flare (top-left panel), during flare (bottom left), and post-flare (bottom right) of the single flare event VAST J005830.0–275132 (CD-28 302) in SB12704. This object was not detected in the model image, but has a  $12\sigma$  detection in one 15-min snapshot image. The radial spikes (bottom left) are from the not-deconvolved point spread function.

time dimension. The advantage of using SNR is to account for local rms variation across the spatial image, for example, the local rms around bright sources is relatively higher and therefore it has larger chance to produce a high noise spike. The peak map is sensitive to variables with a high maximum flux density (e.g. single flare events).

(iii) **Gaussian map**: we created a 1D Gaussian filter kernel with standard deviation of 4 time-steps. We convolved the light curve  $S(x_p, y_p)$  with the Gaussian kernel and stored the maximum value of the convolved light curve at each spatial pixel. The Gaussian map is made up of maximum values measured along time dimension at all spatial pixels, with a size of  $3000 \times 3000$ . As our filter kernel has a standard deviation of 4 time-steps, the Gaussian map is sensitive to  $\sim 1$  h long Gaussian-shape pulsed objects. For a longer-time-scale variable it should be detected in the chi-square map, and a short-time-scale transient should be identified in the peak map. Our Gaussian map can therefore fill the gap between the other two maps.

After we produced a chi-square map, peak map, and Gaussian map for each beam, we selected all local maxima above a certain threshold. We used a relatively conservative threshold equal to 5 times the rms level measured in distributions of individual maps in logarithmic space to suppress the effects of extreme outliers (e.g. artefacts around bright sources). Fig. 6 shows the distribution and the selection threshold of three maps from an example field. We noticed that these maps consist of correlated spatial pixels, and this may affect our statistics of threshold selection. We checked the distributions of values from every 4 (and 8) pixels in maps of a randomly selected field, and the results do not change. We set a relatively strict limit for the separation of two local maxima >30 pixels (75 arcsec) to reduce false detections due to nearby bright sources. We used the coordinates for each local maximum to crossmatch with the model image catalogue. If this local maximum was isolated and not near to any sources in the model image catalogue (i.e. separation >30 arcsec), the coordinates were directly stored in the candidate list. Otherwise we calculated the modulation index mfollowing equation (4), and only selected candidates that meet the metrics described in Section 3.1 (i.e. objects with large m > 0.05,

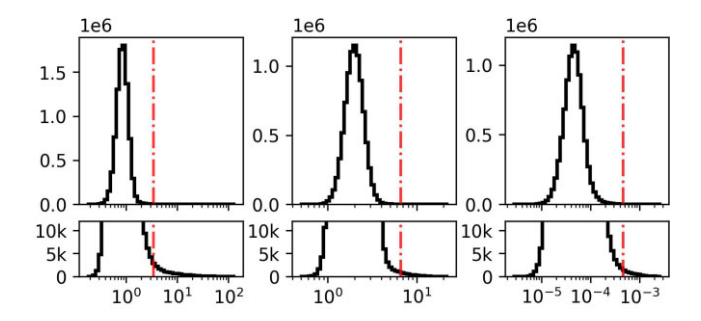


**Figure 6.** Distribution of the chi-square map (left), peak map (middle), and Gaussian map (right) in logarithmic space. The red dash-dot line represents the selection threshold. The bottom panel is a zoomed-in version showing the tail of the distribution.

compact, and close to beam centre). We combined the candidates selected from three maps using a 10 arcsec cross-matching radius, and generated a final candidate list for each beam. All objects in the final candidate list were manually inspected to rule out artefacts. We identified a total of 36 highly variable and transient sources from this analysis, and three of which were not detected in the light-curve analysis. These objects (VAST J005830.0–275132, VAST J044649.5–603408, and VAST J104918.8–250924) are single flare events that were only detected in one or two 15-min model-subtracted snapshot images each (see an example in Fig. 5).

#### 4 RESULTS

We found 35 variable sources using the light-curve analysis approach and 36 variables and transient sources using the statistical map analysis approach, giving a total of 38 unique sources as listed in Table 2. Their light curves are shown in Fig. 7. Note that some observations overlapped and therefore one unique object was detected in multiple observations and has more than one light curve. The flux density  $S_{\rm deep}$  listed in Table 2 is measured in the deep model image without primary beam correction. In the following discussion we also used flux densities from catalogues of standard ASKAP outputs in CASDA, which are measured from primary beam correct, mosaiced image using SELAVY source finder (Whiting & Humphreys 2012). We made a note when the flux density is from the SELAVY catalogue.

To do an initial classification we looked up each object in the SIMBAD Astronomical Data base<sup>10</sup> and the ATNF Pulsar Catalogue<sup>11</sup> (Manchester et al. 2005) using a cross-match radius of 2 arcmin (considering possible proper motion). We searched archival multiwavelength data using a cross-match radius of 10 arcsec from the Wide-field Infrared Survey Explorer (WISE; Wright et al. 2010), the Two Micron All Sky Survey (2MASS; Skrutskie et al. 2006), Gaia (Gaia Collaboration et al. 2018), the Dark Energy Survey (DES; Abbott et al. 2018), and the DESI Legacy Imaging Surveys (Dey et al. 2019). We applied positional corrections for query results using proper motion parameters from Gaia DR3 (when available) or SIMBAD (normally for pulsar counterparts) to make sure the corrected position is within our positional uncertainty. We also generated image cutouts (2 arcmin size) from multiwavelength data (WISE and 2MASS) and inspected radio overlays to confirm the counterparts are matched. We checked previous radio surveys including the GaLactic and Extragalactic All-sky Murchison Widefield Array (GLEAM; Hurley-Walker et al. 2017) at 200 MHz, the Sydney University Molonglo Sky Survey (SUMSS; Mauch et al. 2003) at 843 MHz, and the Rapid ASKAP Continuum Survey (RACS; McConnell et al. 2020; Hale et al. 2021) at 888 MHz. Seven of our sources were found to be known pulsars and eight of them are stellar objects. 22 are likely associated with AGNs or galaxies, and one are unidentified.

For each source we produced full Stokes dynamic spectra with the highest possible time and frequency resolution (10 s and 1 MHz) to investigate the variability behaviour in more detail. We generated dynamic spectra using model-subtracted visibilities (see Section 2.3). We first phased rotated the model-subtracted visibilities from the beam centre to the coordinates of the target object. We averaged the visibilities for each instrumental polarization only using baselines longer than 200 m (to exclude diffuse emission). We then combined the complex visibilities to generate dynamic spectra with full-Stokes parameters. Further, we discussed these variables and transient sources with information from multiwavelength search and dynamic spectra.

#### 4.1 Pulsars

Seven of our highly variable sources are known pulsars, of which three are millisecond pulsars (MSP) in binary systems (see Table 2). Notes on some highlighted pulsars are given further below.

- (i) **PSR J0837+0610** and **PSR J0922+0638** are two bright and well-studied pulsars. Both of them have significant diffractive scintillation reported in literature (e.g. Cordes 1986; Bhat, Gupta & Rao 1998; Thyagarajan et al. 2011; Wu et al. 2022). PSR J0837+0610 is also one of the first known nulling pulsars noticed by Backer (1970). We observed narrow-band scintles in the dynamic spectra (Fig. 8), consistent with what Cordes (1986) reported at a similar frequency (1000 MHz).
- (ii) PSR J1704-6016 has a currently known position of RA  $= 16^{\rm h}59^{\rm m}47^{\rm s}.9$ , Dec.  $= -60^{\circ}12^{'}43^{''}(B1950)$  from timing observations with the Parkes telescope (Newton, Manchester & Cooke 1981). Although this pulsar is about 2.7 arcmin away from VAST J170416.8-601934, we suggest there is an association between them. VAST J170416.8-601934 was detected as 24.4 mJy in SUMSS (843 MHz), 10.6 mJy in RACS (888 MHz), and 2.3 -4.0 mJy (from the SELAVY catalogue) in our data (SB12193, SB12209; 1367.5 MHz). It also shows a faint counterpart in GLEAM (200 MHz). According to this VAST J170416.8-601934 is presumably a steep-spectrum source, with a crude estimation of spectral index  $\alpha \sim -2$  ( $S \propto v^{\alpha}$ ). VAST J170416.8–601934 has no counterpart at other wavelengths including infrared, optical, or  $\gamma$ -ray. We observed narrow-band scintles in the dynamic spectra, suggesting its compact nature. All of earlier properties are consistent with a pulsar. PSR J1704-6016 was reported as 23 mJy at 400 MHz by Taylor, Manchester & Lyne (1993). However, there is no source at its catalogued position from any of earlier radio continuum surveys. We therefore suggest there is a position error in the original pulsar catalogue, and PSR J1704-6016 is the counterpart of VAST J170416.8-601934.
- (iii) **PSR J2039–5617** is a known  $\gamma$ -ray source and was recently confirmed as a 2.6 ms radio pulsar with orbital period of about 5.5 h (Clark et al. 2021; Corongiu et al. 2021). This orbital modulation causes radio emission obscured for about half the orbit roughly consistent with our light curve in Fig. 7 (covering a full orbit phase range with a rising trend at the end of the observation SB9351). PSR

<sup>10</sup>http://simbad.cds.unistra.fr/simbad/

<sup>11</sup> https://www.atnf.csiro.au/people/pulsar/psrcat/

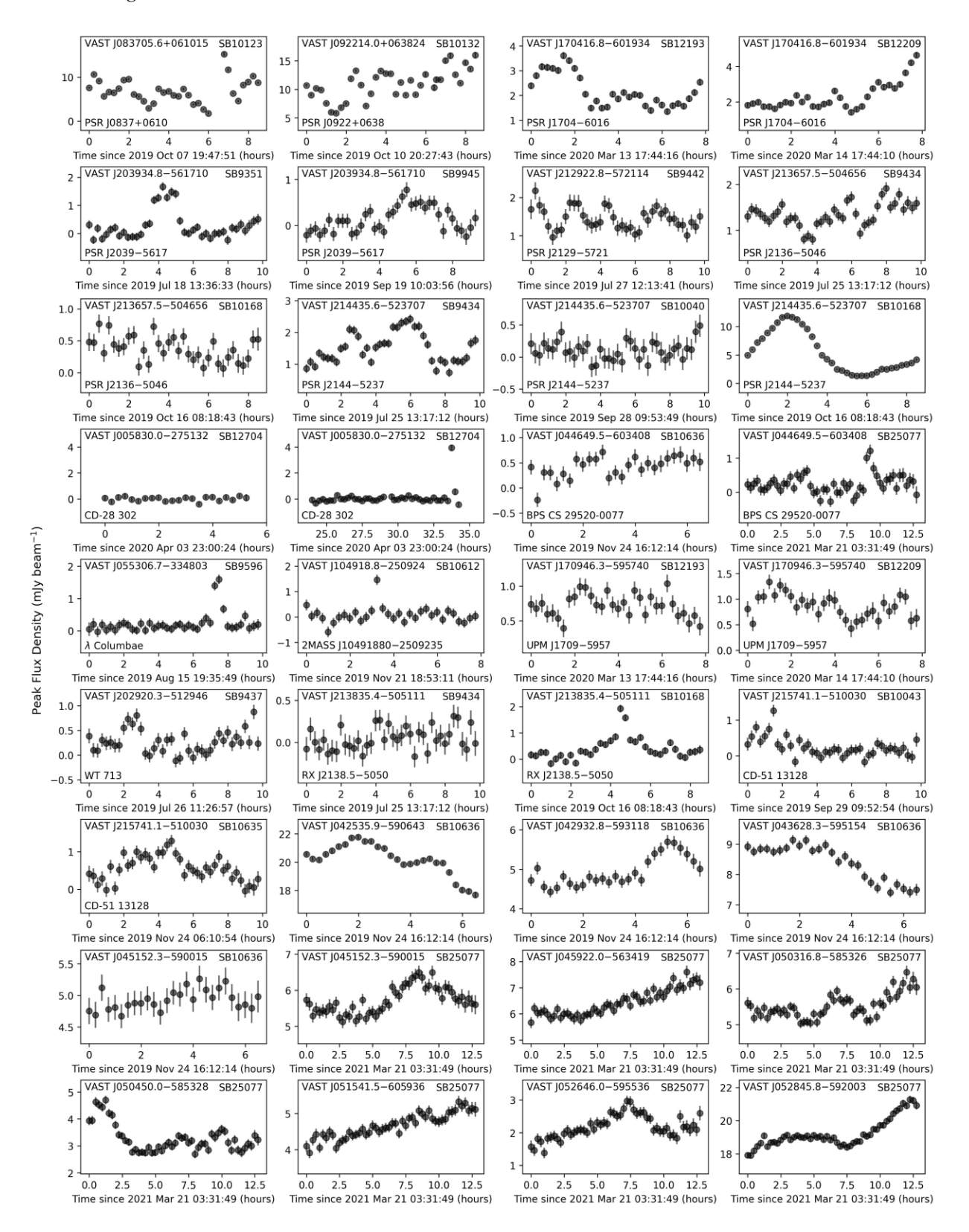


Figure 7. Light curves of variables and transient objects identified in our survey. The start time shown in x-axis label is the UTC time. These light curves follows the order of objects listed in Table 2, but we moved sources in S190814bv fields to the end as they normally have  $\sim 10$  observations.

J2039—5617 shows significant variation in pulsed amplitude and has been detected in the VAST Phase I Pilot Survey (Murphy et al. 2021) as a highly variable source on longer time-scales (~days).

(iv) **PSR J2144–5237** is a 5 ms pulsar in a binary system (orbital period of  $\sim$ 10 d) identified by Bhattacharyya et al. (2016, 2019) using the Giant Metrewave Radio Telescope (GMRT). They suggested

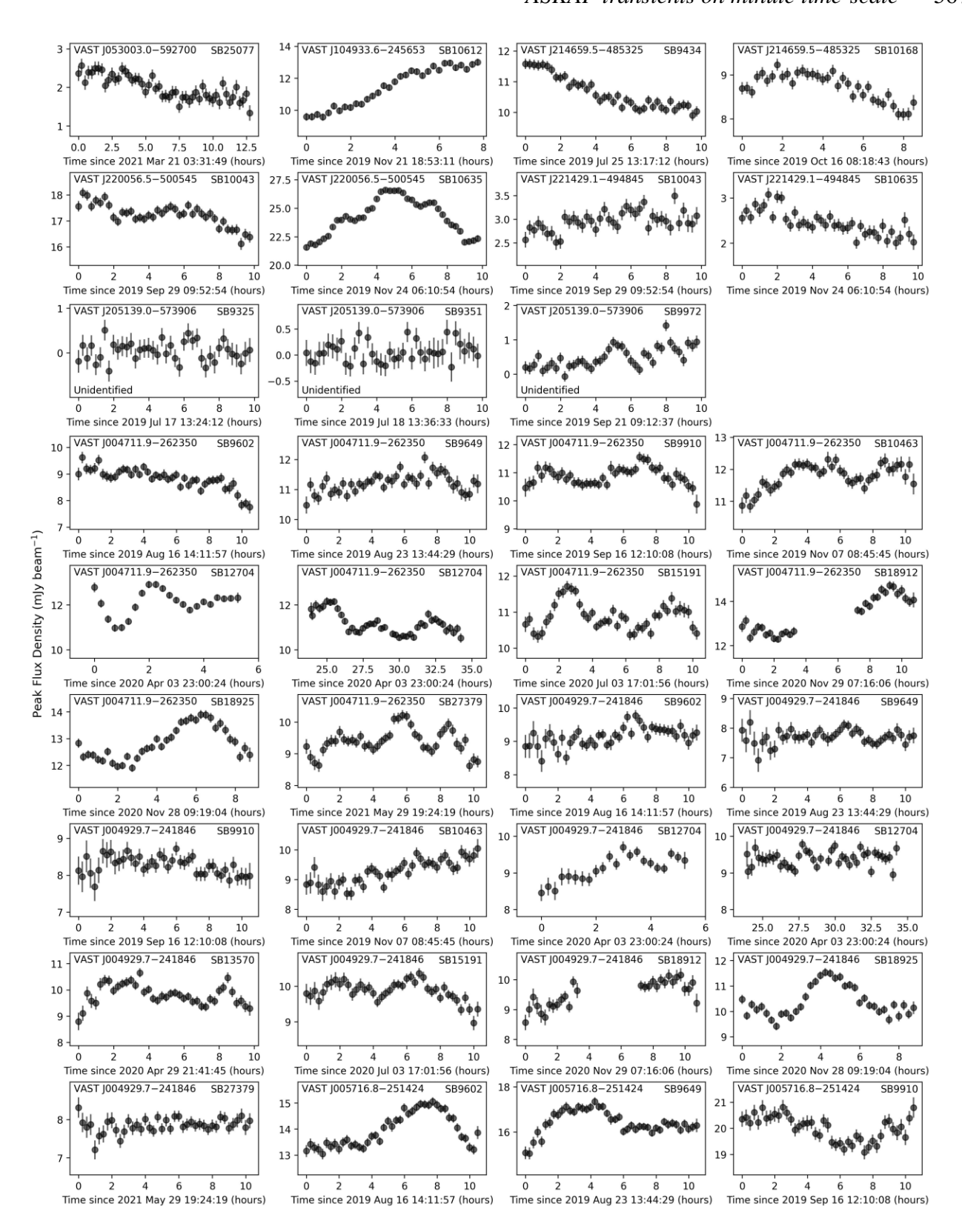


Figure 7. (continued).

a 'redback' system for this object based on companion mass, but found no sign of eclipses in their timing data. PSR J2144-5237 was detected in two of our data sets (SB9434 and SB10168), showing clear frequency structure in the dynamic spectra. It has broad-band

scintles (comparable with the observing bandwidth of 144 MHz) at SB10168 (1367.5 MHz) and relatively narrow-band scintles at SB9434 (943.5 MHz). This object has also been detected in VAST Phase I Pilot Survey.

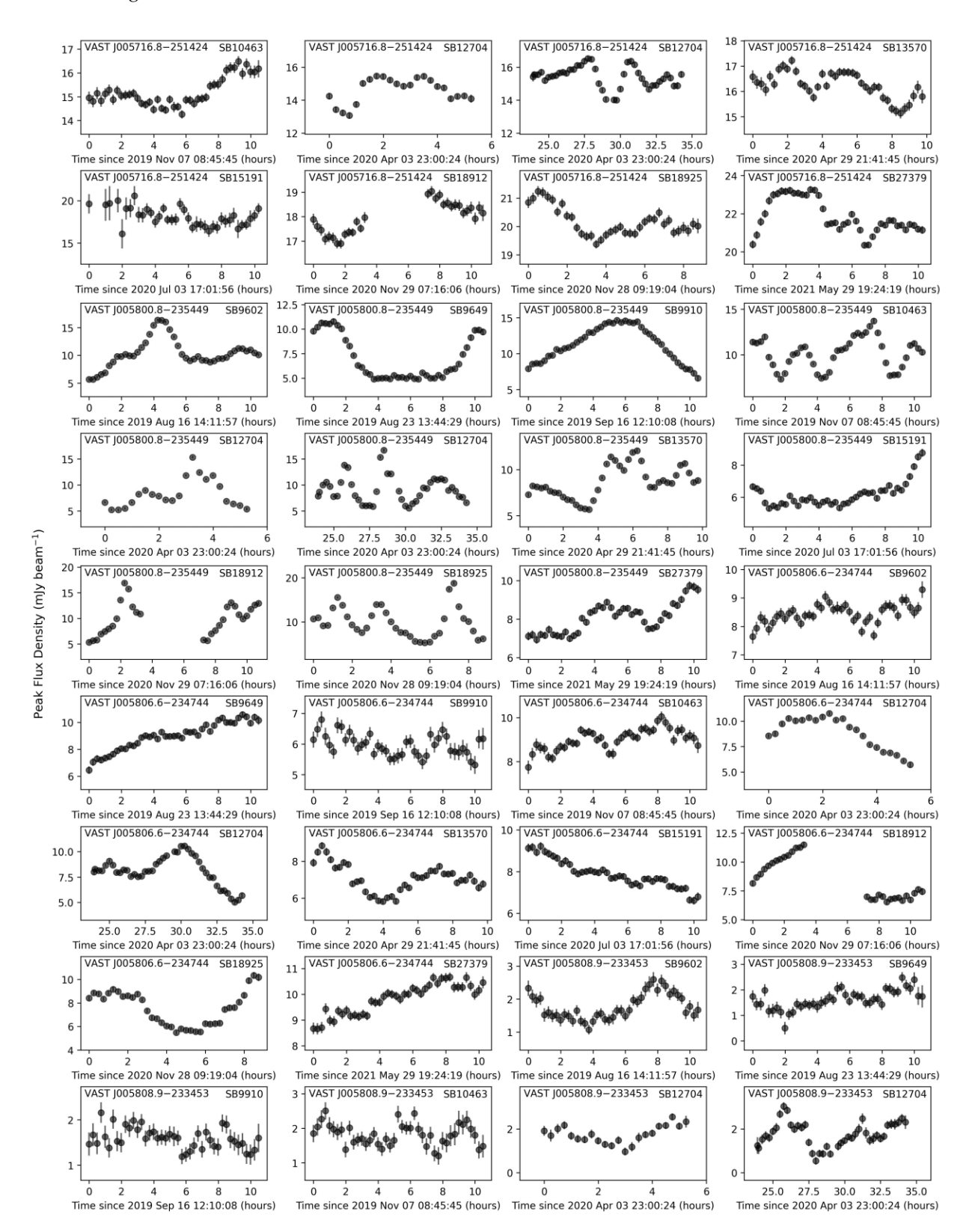


Figure 7. (continued).

In summary, we observed narrow-band scintles in the dynamic spectra from six of seven pulsars (see Fig. 8 as an example). The remaining object, PSR J2039-5617, is an eclipsing MSP. Pulsars

are generally most extreme variables in our sample, with higher  $\eta$  and m than most of stars and AGNs/galaxies (as shown in Fig. 4).

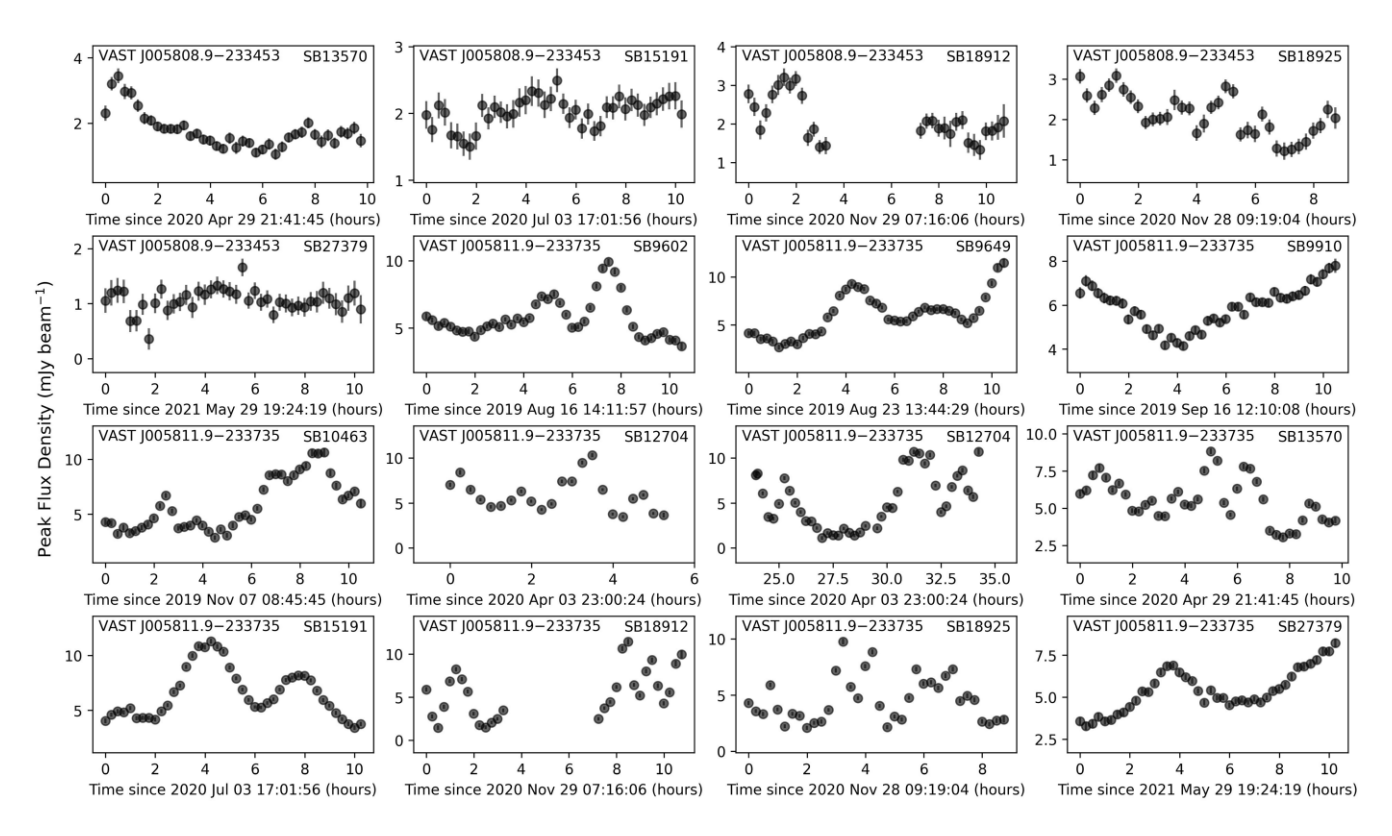


Figure 7. (continued).

#### 4.2 Stars

Eight of our identified transients are radio stars. Five of the stars are M dwarfs and one (CD-51 13128) is an M dwarf binary. One ( $\lambda$  Columbae) is classed as a B5V star. The other star (UPM J1709–5957) do not have classifications. Six of the eight stars have previously been identified as X-ray stars, while the other two are coincident with X-ray sources. Here we provide a brief description of each source.

- (i) **CD-28 302** is a single-line spectroscopic binary (Fouqué et al. 2018) where the main component is a dM4 star (e.g. Houdebine et al. 2019). It was identified as a non-single star in *Gaia* DR3 with an orbital period of  $\sim$ 147.0 d (Gaia Collaboration et al. 2016, 2022). The source has not been definitely identified as an X-ray source; however, there are detections of an X-ray source within a few arcseconds of the source position by *ROSAT* (Voges et al. 1999), *XMM–Newton* (e.g. Traulsen et al. 2020) and *Chandra* (Evans et al. 2010). CD-28 302 has not previously been identified as a radio star. The *Gaia* DR3 parallax is 84.98  $\pm$  0.46 mas, with a distance of 11.77 $_{-0.07}^{+0.07}$  pc (Bailer-Jones et al. 2021).
- (ii) BPS CS 29520–0077 is a single M1.5V star (e.g. Riaz, Gizis & Harvin 2006; Malo et al. 2014). It was noted to have strong Calcium H and K emission lines by Beers et al. (1996) and is a known X-ray star (Freund et al. 2018). This object was detected in the radio by Rigney et al. (2022) using ASKAP. They measured a peak Stokes I flux density of  $0.25 \pm 0.01$  mJy beam $^{-1}$  over the full 13 h integration, and identified the same radio peak we show here after dividing the 13 h observation into 10 min slices. Rigney et al. (2022) used the same procedure as described in this work to investigate the short-time-scale light curve. The Gaia DR3 parallax is  $40.73 \pm 0.01$  mas, with a distance of  $24.542^{+0.006}_{-0.008}$  pc (Bailer-Jones et al. 2021).

- (iii)  $\lambda$  Columbae is a variable B5V star (e.g. Rimmer 1930; Johnson & Mitchell 1975). It was identified as a rotating ellipsoidal variable with a period of 1.3 d by Watson, Henden & Price (2006), possibly indicating that  $\lambda$  Columbae is a tight binary. It is also a known X-ray star (Voges et al. 1999).  $\lambda$  Columbae has not previously been identified as a radio star. The *Gaia* DR3 parallax is 9.47  $\pm$  0.09 mas, with a distance of 105.4  $\pm$  0.9 pc (Bailer-Jones et al. 2021).
- (iv) **2MASS J10491880–2509235** is a single, young, lithium rich M4.9 star demonstrating strong H-alpha emission (Murphy, Lawson & Bento 2015), and has not previously been reported as radio loud. The star has also been associated with X-ray activity by *ROSAT* (Voges et al. 1999), *XMM–Newton* (e.g. Traulsen et al. 2020) and *Chandra* (Evans et al. 2010) that is consistent with a young age (Murphy et al. 2015). The *Gaia* DR3 parallax is 9.50  $\pm$  0.04 mas, with a distance of 104.6 $^{+0.4}_{-0.6}$  pc (Bailer-Jones et al. 2021).
- (v) **UPM J1709 5957** does not have a stellar classification and has not been previously reported as radio loud. It is a known X-ray star, detected by *ROSAT* (Haakonsen & Rutledge 2009) and it was identified as a long-period variable by Gaia Collaboration et al. (2022). This source does not have a *Gaia* parallax or distance measurement. The photometric distance was estimated to be  $14.13 \pm 2.77$  pc by Finch et al. (2014).
- (vi) **WT 713** is a photometrically classified M dwarf (Sebastian et al. 2021) and has not been previously reported as radio loud. It was identified as an X-ray star using *ROSAT* by Freund et al. (2022). The *Gaia* DR3 parallax is  $26.61 \pm 0.02$  mas, with a distance of  $37.49^{+0.04}_{-0.03}$  pc (Bailer-Jones et al. 2021).
- (vii) **RX J2138.5–5050** is an M7/8 ultra-cool dwarf candidate (Lee, Song & Murphy 2022) and an eruptive variable detected by *TESS* (Günther et al. 2020). It was identified as an X-ray star using *ROSAT* by Freund et al. (2022). The *Gaia* DR3 parallax is

**Table 2.** Transients and variables identified in our survey. We list their coordinates, variability metrics  $\eta$  and m, and flux density  $S_{\text{deep}}$  (as described in Section 3.1). We list all of observations that covered the source location, and mark observations where we detected no variable behaviour as asterisk (\*). The listed beam has the beam centre closest to the source location. We provide the SIMBAD ID, the *WISE* cross-ID, or the LS object ID from the DESI Legacy Imaging Survey DR8 catalogue (Dey et al. 2019). We list the mean and standard deviation of the photometric redshift distributions when available (from Duncan 2022).

Name	RA (J2000) (hh:mm:ss)	Dec. (J2000) (dd:mm:ss)	η	m	$S_{\text{deep}}$ (mJy beam <sup>-1</sup> )	SBID (beam number)	Identification	Notes
Pulsars								
VAST J083705.6+061015	08:37:05.68	+06:10:15.63	106.43	0.34	$7.19 \pm 0.06$	10 123 (B5)	PSR J0837+0610	Nulling pulsar
VAST J092214.0+063824	09:22:14.03	+06:38:24.17	115.44	0.22	$10.86 \pm 0.06$	10 132 (B4)	PSR J0922+0638	-
VAST J170416.8-601934	17:04:16.85	-60:19:34.79	26.03	0.26	$2.58 \pm 0.03$	12 193 (B10); 12 209 (B3)	PSR J1704-6016	-
VAST J203934.8-561710	20:39:34.86	-56:17:10.37	12.96	0.90	$0.28 \pm 0.03$	9351 (B14); 9945 (B4)*	PSR J2039-5617	Eclipsing MSP
VAST J212922.8-572114	21:29:22.80	-57:21:14.41	2.96	0.14	$1.45 \pm 0.05$	9442 (B4)	PSR J2129-5721	MSP
VAST J213657.5-504656	21:36:57.58	-50:46:56.83	4.40	0.13	$1.34 \pm 0.03$	9434 (B21); 10 168 (B14)	PSR J2136-5046	-
VAST J214435.6-523707	21:44:35.67	-52:37:07.73	12.91	0.22	$1.53 \pm 0.03$	9434 (B10); 10 040 (B30)*; 10 168 (B4)	PSR J2144-5237	MSP
Stars								
VAST J005830.0-275132	00:58:30.03	-27:51:32.65	5.91	_	-	12 704 (B5) <sup>a</sup>	CD-28 302	dM4
VAST J044649.5-603408	04:46:49.50	-60:34:08.13	2.32	1.06	$0.26 \pm 0.04$	25 077 (B32); 10 636 (B29)*	BPS CS 29520-0077 <sup>b</sup>	M1.5V
VAST J055306.7-334803	05:53:06.78	-33:48:03.50	5.04	0.65	$0.23 \pm 0.03$	9596 (B14)	λ Columbae	B5V
VAST J104918.8-250924	10:49:18.83	-25:09:24.51	2.59	-	0.25 ± 0.05	10 612 (B21)	2MASS J10491880-2509235	M4.9
VAST J170946.3-595740	17:09:46.30	-59:57:40.26	2.48	0.17	$0.88 \pm 0.03$	12 209 (B9); 12 193 (B9)*	UPM J1709-5957	_
VAST J202920.3-512946	20:29:20.30	-51:29:46.37	3.05	0.39	$0.30 \pm 0.04$	9437 (B15)	WT 713	M dwarf
VAST J213835.4-505111	21:38:35.49	-50:51:11.64	5.41	0.53	$0.31 \pm 0.02$	10 168 (B14); 9434 (B21)*	RX J2138.5-5050	M7/8 candidate
VAST J215741.1-510030	21:57:41.12	-51:00:30.72	3.62	0.28	$0.58 \pm 0.03$	10 635 (B19); 10 043 (B13)*	CD-51 13 128	M dwarf binary
AGN/galaxies								•
VAST J004711.9-262350	00:47:11.95	-26:23:50.62	22.97	0.06	$9.69 \pm 0.03$	S190814bv fields (B8)	WISEA J004712.05-262350.5	Quasar $(z = 1.11 \pm 0.47)$
VAST J004929.7-241846	00:49:29.79	-24:18:46.67	16.09	0.05	$10.34 \pm 0.04$	\$190814bv fields (B26)	3HSP J004929.9–241844	Blazar ( $z = 0.78 \pm 0.50$ )
VAST J005716.8-251424	00:57:16.83	-25:14:24.47	16.93	0.05	$12.98 \pm 0.04$	\$190814bv fields (B22)	WISEA J005716.92-251424.4	See Wang et al. (2021)
VAST J005800.8-235449	00:58:00.87	-23:54:49.03	162.47	0.25	$8.80 \pm 0.04$	\$190814bv fields (B29)	WISEA J005800.99-4235448.0	See Wang et al. (2021)
VAST J005806.6-234744	00:58:06.69	-23:47:44.47	59.42	0.15	$8.40 \pm 0.04$	\$190814bv fields (B29)	LS DR8 8 000 197 415 002 484	See Wang et al. (2021)
VAST J005808.9-233453	00:58:08.93	-23:34:53.77	6.22	0.13	$1.47 \pm 0.04$	\$190814bv fields (B24)	WISEA J005808.68-233453.0	See Wang et al. (2021)
VAST J005808.9 233435 VAST J005811.9-233735	00:58:11.96	-23:37:35.69	176.56	0.41	$4.89 \pm 0.03$	\$190814bv fields (B34)	WISEA J005812.03—233735.6	See Wang et al. (2021)
VAST J042535.9-590643	04:25:35.96	-59:06:43.85	45.41	0.06	$20.42 \pm 0.03$	10 636 (B31)	WISEA J042535.97-590642.4	Quasar
VAST J042932.8-593118	04:29:32.89	-59:31:18.61	5.35	0.06	$4.98 \pm 0.05$	10 636 (B32)	LS-DR8 8 000 045 911 001 631	Quasar $(z = 2.42 \pm 0.36)$
VAST J043628.3-595154	04:36:28.34	-59:51:54.25	13.47	0.06	$8.66 \pm 0.04$	10 636 (B32) 10 636 (B33)	2MASX J04362838-5951531	Galaxy ( $z = 0.058 \pm 0.021$ )
VAST J045028.3 599134 VAST J045152.3 – 590015	04:51:52.31	-59:00:15.22	5.34	0.06	$5.75 \pm 0.03$	25 077 (B34); 10 636 (B35)*	WISEA J045152.41 – 590014.8	Quasar $(z = 0.036 \pm 0.021)$
VAST J045922.0-563419	04:59:22.05	-56:34:19.04	5.91	0.07	$6.52 \pm 0.05$	25 077 (B34), 10 030 (B33)* 25 077 (B16)	-	Quasar (2 = 1.50 ± 0.57)
VAST J050316.8-585326	05:03:16.81	-58:53:26.42	5.25	0.06	$5.57 \pm 0.04$	25 077 (B10) 25 077 (B0)	WISEA J050316.89-585325.1	Galaxy ( $z = 0.85 \pm 0.09$ )
VAST J050450.0-585328	05:04:50.04	-58:53:28.51	13.03	0.13	$3.37 \pm 0.04$ $3.31 \pm 0.03$	25 077 (B0) 25 077 (B0)	WISEA J050510.89=385325.1 WISEA J050450.20=585328.2	Galaxy ( $z = 0.03 \pm 0.09$ ) Galaxy ( $z = 0.17 \pm 0.02$ )
VAST J050450.0-585528 VAST J051541.5-605936	05:15:41.52	-60:59:36.16	5.68	0.15	$4.74 \pm 0.03$	25 077 (B9)	WISEA J050450.20-565526.2 WISEA J051541.65-605935.9	Quasar $(z = 0.17 \pm 0.02)$
VAST J051541.5-005950 VAST J052646.0-595536	05:15:41.32	-59:55:36.05	5.37	0.06	$4.74 \pm 0.03$ $2.22 \pm 0.03$	25 077 (B23)	WISEA J051541.05-005955.9 WISEA J052646.15-595535.7	Galaxy $(z = 0.29 \pm 0.02)$
VAST J052845.8-592003	05:28:45.86	-59:20:03.60	19.15	0.11	$11.11 \pm 0.03$	25 077 (B23) 25 077 (B7)	4FGL J0528.7—5920	Blazar $(z = 0.29 \pm 0.02)$
VAST J052845.8-592005 VAST J053003.0-592700	05:30:03.01	-59:27:00.75	3.34	0.03	$1.99 \pm 0.03$	25 077 (B27) 25 077 (B22)	WISEA J053003.05-592701.2	Galaxy ( $z = 1.13 \pm 0.36$ )
VAST J033003.0-392700 VAST J104933.6-245653	10:49:33.63	-39:27:00.73 -24:56:53.30	38.84	0.10	$1.99 \pm 0.03$ $12.37 \pm 0.04$	10 612 (B21)	WISEA J033003.03-392701.2 WISEA J104933.63-245651.8	Quasar $(z = 1.13 \pm 0.36)$
VAST J104955.0-245055 VAST J214659.5-485325	21:46:59.54	-48:53:25.94	9.69	0.10	$12.37 \pm 0.04$ $10.81 \pm 0.04$	9434 (B35); 10 168 (B34)*	WISEA J104955.05-245051.6 WISEA J214659.48-485325.4	Galaxy ( $z = 1.01 \pm 0.67$ )
VAST J220056.5-500545	22:00:56.52	-50:05:45.53	76.02	0.05	$24.25 \pm 0.08$	10 635 (B26); 10 043 (B25)*	LS-DR8 8 000 078 211 000 459	Quasar $(z = 1.01 \pm 0.07)$
VAST J220030.3-300343 VAST J221429.1-494845	22:14:29.13	-30:03:43.33 -49:48:45.60	4.21	0.00	$2.44 \pm 0.03$	10 635 (B26); 10 043 (B28)* 10 635 (B29); 10 043 (B28)*	WISEA J221429.13-494845.1	Quasar $(z = 1.27 \pm 0.47)$ Quasar
	22.17.27.13	77.70.73.00	7.21	0.10	2.77 ± 0.03	10 055 (127), 10 075 (120)*	,,,,,,,,,,,,,,,,,,,,,,,,,,,,,,,,,,,,,,	Zaman
Unidentified VAST J205139.0-573906	20:51:39.00	-57:39:06.38	3.32	0.32	$0.50\pm0.03$	9972 (B29); 9325 (B25)*; 9351 (B4)*	-	?

Notes.<sup>a</sup> No detection in the time-averaged model image. Only detected one single flare in SB12704 although covered by other S190814bv fields.

<sup>&</sup>lt;sup>b</sup> Detected in the original paper by Rigney et al. (2022).

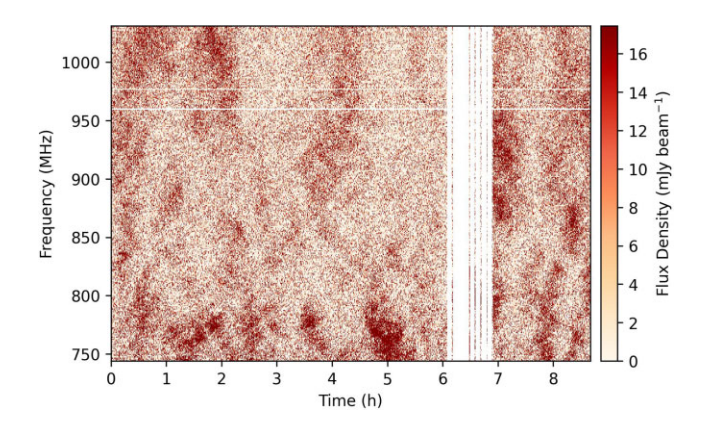


**Figure 8.** An example dynamic spectrum from one of identified pulsars (PSR J0837+0610 in SB10123). The narrow-band scintles are clearly shown. The flagged data are represented as white colour.

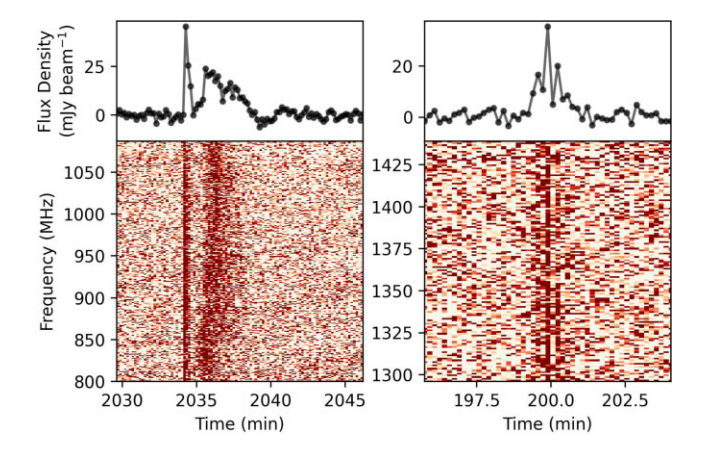


**Figure 9.** The total intensity dynamic spectra of two flaring stars CD-28 302 (left panel) and 2MASS J10491880–2509235 (right panel). The temporal and spectral resolution are 10 s and 1 MHz, respectively.

 $22.09 \pm 0.20$  mas, with a distance of  $44.96^{+0.3}_{-0.4}$  pc (Bailer-Jones et al. 2021).

(viii) **CD-51 13128** is an M dwarf binary with a 1.24 d period (Jeffries & Bromage 1993), with a third white dwarf component in a wide orbit around the M dwarf pair (Wegner 1981). It has been identified as an X-ray source using *ROSAT* (Haakonsen & Rutledge 2009; Freund et al. 2022). The *Gaia* DR3 parallax is  $67.27 \pm 0.02$  mas, with a distance of  $14.858^{+0.004}_{-0.005}$  pc (Bailer-Jones et al. 2021).

As shown in Fig. 7, their light curves have diverse morphologies and flare durations. After checked their dynamic spectra, two stars have even shorter flares than 15 min (see Fig. 9). One is CD-28 302 showing a ~5 min multicomponent burst reaching a flux density of 45.6 mJy beam<sup>-1</sup>; another one is 2MASS J10491880—2509235 showing a 100 per cent circularly polarized burst lasting about 1 min and reaching a flux density of 35.5 mJy beam<sup>-1</sup>. Table 3 lists the estimated variability time-scales of all stars. They are approximate values identified by eye from dynamic spectra and 15-min light curves. The listed radio luminosities are calculated using the maximum flux density measured in the 15-min light curves or 10-s light curves if their variability time-scales are shorter than 15 min. We present more discussions in Section 5.1.2.

**Table 3.** Table of detected radio stars. We list the estimated radio luminosities and variability time-scales.

Name	Radio luminosity (erg s <sup>-1</sup> Hz <sup>-1</sup> )	Time-scale
CD-28 302	$7.6 \times 10^{15}$	30 s; 4 min
BPS CS 29520-0077	$8.8 \times 10^{14}$	$\sim$ 1 h
λ Columbae	$2.1 \times 10^{16}$	$\sim$ 1 h
2MASS J10491880-2509235	$4.6 \times 10^{17}$	1 min
UPM J1709-5957	$3.2 \times 10^{14}$	a few hours
WT 713	$1.5 \times 10^{15}$	$\sim$ 1 h
RX J2138.5-5050	$4.7 \times 10^{15}$	$\sim$ 1 h
CD-51 13 128	$3.4 \times 10^{14}$	a few hours

## 4.3 AGN/galaxies

We found 23 variable sources that were not identified as known pulsars or stars. For further investigation we checked the *WISE* colours for those sources with a *WISE* counterpart, the photometric redshift from the DESI Legacy Imaging Surveys DR8 catalogue (Duncan 2022), and the Million Quasars (Milliquas) catalogue (v7.10; Flesch 2015, 2021). Their multiwavelength properties are summarized in Table 2.

We found the majority of these objects (21) are associated with catalogued AGN or galaxies. The remaining two objects lack any obvious optical or infrared counterparts and are yet to be identified. One of these VAST J045922.0–563419 was detected in SUMSS (7.7  $\pm$  0.8 mJy) and hence is also likely associated with an AGN or galaxy. We present more discussions in Section 5.2.

#### 4.4 An unclassified transient

The remaining object, VAST J205139.0-573906, has no multiwavelength counterparts and was not detected in any archival radio surveys including GLEAM, SUMSS, and RACS. It was only detected in a single ASKAP observation SB9972, with a flux density of  $0.58 \pm 0.03 \,\mathrm{mJy\,beam^{-1}}$  (from the SELAVY catalogue) at 1367.5 MHz. This area has been covered by three other 10h ASKAP observations, and the non-detection implies a  $3\sigma$  limit of 0.13-0.15 mJy beam<sup>-1</sup> at 943.5 MHz (SB9325 and SB9351) and 0.17 mJy beam<sup>-1</sup> at 1367.5 MHz (near the edge of SB9992). For the detected epoch SB9972, the intra-observation analysis shows a high variability ( $m \sim 0.32$ ) on time-scales of minutes to hours (see Fig. 7) - faster and more extreme than most variables associated with AGN/galaxies. VAST J205139.0-573906 has strong linear polarization of 38 per cent, with a rotation measure (RM) of about 8.4 rad m<sup>-2</sup>. It also has a  $4\sigma$  peak (0.13  $\pm$  0.03 mJy beam<sup>-1</sup>) in the Stokes V image, suggesting a potential high fractional circular polarization ( $\sim$ 22 per cent) if the detection is real. Further observations are ongoing to determine the nature.

## 5 DISCUSSION

## 5.1 The origin of variability in our sample

## 5.1.1 Pulsars

For six of seven pulsars we observed narrow-band scintles in their dynamic spectra (as shown in Fig. 8), with the only exception being PSR J2039-5617 whose variability is presumably from eclipses. This shows that diffractive scintillation is the dominant reason of pulsar variability on this time-scale at this observing frequency.

# 5676 *Y. Wang et al.*

This is not unexpected as refractive interstellar scintillation usually appears on much longer time-scales (e.g. ≳days). The presence of high quality scintles in the dynamic spectra also highlights the possibility of estimating screen distances (for pulsars with known proper motion) with ASKAP. More discoveries would improve our understanding of local scattering environment and the origins of scintillation.

From the ATNF Pulsar Catalogue, we found 14 pulsars that were detected in the 10-h deep ASKAP image but not selected by our pipeline, suggesting about one third of pulsars vary on 15-min timescales based on our selection criteria. These 'non-varying' pulsars generally have a much larger dispersion measure and fainter than our identified pulsars, making it harder to detect any variations. Future dedicated investigation is required to quantify pulsar behaviours on short time-scales.

#### 5.1.2 Stars

The majority of our identified stars are M-dwarf stars, which are known to produce radio flares on time-scales ranging from seconds to hours due to strong magnetic fields – similar to what we detected (e.g. Dulk 1985; Villadsen & Hallinan 2019). The radio luminosity of our identified stars ranges from  $10^{14}$  to  $10^{17}$  erg s<sup>-1</sup> Hz<sup>-1</sup> (see Table 3), with the majority being around  $10^{15}$  erg s<sup>-1</sup> Hz<sup>-1</sup>. These values are consistent with other studies at similar observing frequencies (e.g. Villadsen & Hallinan 2019; Pritchard et al. 2021, Pritchard et al. 2023, *submitted*).

In the left panel of Fig. 9 we show a Stokes I dynamic spectrum of a multicomponent burst from CD-28 302 reaching a flux density of 45.6 mJy beam<sup>-1</sup>. The first component is elliptically polarized with 90 per cent circular polarization and 10 per cent linear polarization and lasts 30 s, while the second component is 100 per cent circularly polarized and lasts for about 4 min with a positive frequency drift rate of 3.3 MHz s<sup>-1</sup>. The high-fractional circular polarization and presence of elliptical polarization suggests the emission is produced by the electron cyclotron maser instability (ECMI). The polarization properties and burst morphology are similar to the Type IV burst detected from Proxima Centauri by Zic et al. (2020), though with a significantly shorter delay between burst components.

We also detected a single, 100 per cent circularly polarized burst lasting ~1 h from λ Columbae, a B5V star. B-type stars are not typical radio emitters, lacking a magnetic dynamo mechanism and thus a means to produce the strong magnetic fields associated with highly circularly polarized radio emission. One possible explanation is that the emission originates from an undiscovered binary companion that is a more typical radio emitter. As mentioned in Section 4.2,  $\lambda$ Columbae is likely a tight binary, though Jerzykiewicz & Sterken (1993) found that the mass of any tidally influential companion must be less than  $1 M_{\odot}$  and rules out tidal effects as a cause of variability. We note that the binary system with a companion like this would have an extreme mass ratio  $q \lesssim 0.2$  – uncommon in existing observations (Moe & Di Stefano 2017). However, similar systems have been detected previously and provided valuable information for understanding stellar formations and evolution (e.g. Moe & Di Stefano 2015). The low detection number of extreme mass-ratio systems may also be a result of technique limitations. We therefore cannot rule out the presence of a sub-stellar companion in this system, and it is possible that a more typical radio emitter such as a K- or M-type dwarf may be the source of radio emission. We note that the estimated radio luminosity of  $\lambda$  Columbae is consistent with other M-dwarf stars in our samples. Another possibility is that  $\lambda$  Columbae is a magnetic chemically peculiar star that has not yet been identified. These stars are known to produce rotationally modulated pulses of circularly polarized radio emission (e.g. Trigilio et al. 2000; Leto et al. 2020; Das et al. 2022) over time-scales that align with the observed  $\sim 1$ -h burst.

#### 5.1.3 AGN/galaxies

For the 22 objects associated with AGN or galaxies, five of them are extreme IHVs discovered previously by Wang et al. (2021). We excluded these five known objects from this discussion.

We first consider an intrinsic origin for the variability of the remaining 17 sources. If we consider the incoherent emission process, we can estimate the brightness temperature  $T_b$  following the Rayleigh–Jeans law. We cannot determine a reliable characteristic time-scale since most of objects varies slowly in a monotonically increasing or decreasing way with a relatively low modulation index  $\leq 10$  per cent. Instead we consider the maximum flux density change  $\Delta S$  in the corresponding time interval  $\Delta t$ . We obtain an expression for brightness temperature as follows

$$T_b = \frac{d^2 \Delta S}{2k \nu^2 \Delta t^2},\tag{5}$$

where d is the distance estimated using photometric redshift (as listed in Table 2) in cosmology of  $H_0 = 70 \, \mathrm{km \, s^{-1} Mpc^{-1}}$ , k is the Boltzmann constant and  $\nu$  is the observing frequency. We found the estimated brightness temperature is about  $10^{16} - 10^{19} \, \mathrm{K}$ , greatly exceeding the inverse Compton limit  $T_b \sim 10^{12} \, \mathrm{K}$  for inconherent synchrotron emission (Kellermann & Pauliny-Toth 1969). Even for a relativistic source (which is true for some AGNs), it would require a Doppler boosting factor  $\sim 100$  to explain the observed luminosity changes (Blazar normally has a factor of  $\sim 10$ ; Hovatta et al. 2009). We conclude that the observed variations are not likely to be intrinsic. This is not surprising given our observing frequency ( $\sim$ GHz) and time-scale (15 min).

If we consider the variability to have an extrinsic origin (i.e. propagation effects), we can calculate the expected scintillation transition frequency using NE2001 (Cordes & Lazio 2002). We then estimated the variability level from refractive scintillation based on Walker (1998). We find the expected point-source modulation index is  $\sim\!\!25$  per cent -40 per cent and the scintillation time-scale is  $\sim\!\!5$  -20 d for the lines-of-sight of these objects. This is much slower than what we observed, suggesting that normal scintillation caused by Kolmogorov turbulence in the diffuse, ionized ISM is unlikely to explain these variables.

Considering the variability time-scales we observed (~hours), the most likely explanation is enhanced scintillation caused by nearby plasma screens - similar to (although slower than) the five known IHVs reported by Wang et al. (2021). The scintillation time-scale for weak or refractive scattering increases with distance between the scattering screen and the observer (Narayan 1992), and a relatively local scintillating screen can explain the variability time-scales of these objects. For the origin of local scintillation screen, Walker et al. (2017) proposed that extreme scintillation may be associated with hot stars in the solar neighbourhood, and the scattering plasma is from thin skins on tiny molecular gas clouds surrounding the star. In our sample there are two variables offset by 20 - 30 arcsec from two nearby stars (VAST J042932.8-593118 and TYC 8515-1281-1; VAST J053003.0-592700 and TYC 8530-1065-1). Both stars are  $\sim$ 11 mag at B band and  $\sim$ 300 pc away from us. We find a surface density of ~0.001 per arcmin<sup>2</sup> for bright stars at this level, and would expect to find 0.001 stars within 1 arcmin<sup>2</sup> area around a random

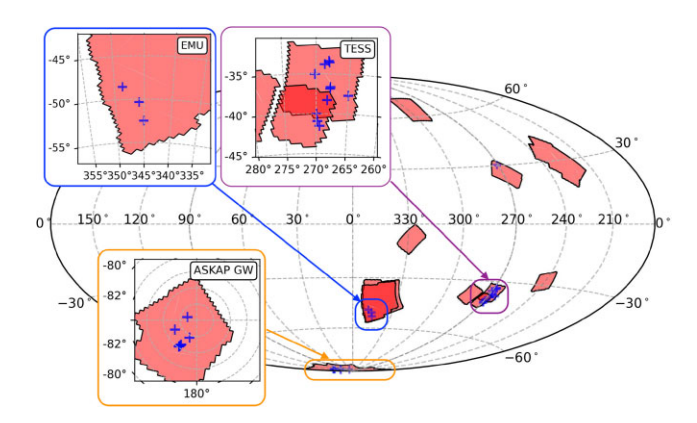


**Figure 10.** Sky distribution of scintillating AGNs we identified (shown as blue '+' marker). The sky map is plotted with Galactic coordinates, overlaid with red shadow representing the sky region covered by this survey. The zoommed-in insets show three regions clustered by scintillating AGNs.

object. However, we found 2 bright stars near these 22 objects with a separation of <30 arcsec, which is two orders of magnitude higher than the expected value. More observations (especially at different observing frequencies and on different date of year) are needed to constrain the screen kinematics and distance, and to confirm or rule out this association.

## 5.2 Sky distribution of AGN/galaxies

In the S190814bv field, Wang et al. (2021) discovered five extreme scintillators in a linear arrangement in the sky, revealing a common long (>1.7 degrees), thin  $(1-4 \, \text{arcmin})$ , and straight plasma screen near to Earth (a few pc). This is the first time to known the geometry of a discrete, local cloud that causes extreme scintillation, raising a question of how common the similar plasma screen is in the solar neighbourhood.

We searched a larger sky area in this work, and discovered 17 new scintillating objects. We found no obvious alignment for these new scintillators (see Fig. 10). Wang et al. (2021) calculated the rate of recognizing a similar filament is at least 16 per cent when discovered one scintillator. We therefore expect to recognize at least 2 or 3 similar filamentary screens if they are responsible for the variations. Since we do not find any alignment, it is likely that these plasma screens are much shorter than the one found previously, or they are not in a straight filamentary shape. We detected two new variables (VAST J004711.9-262350 and VAST J004929.7-241846) in the original S190814bv field and noticed they are not located near or within the line. We analysed annual modulation of scintillation rates of the two new variables using the same method as Wang et al. (2021). The screen kinematics of the two variables are not well constrained as their variations are less extreme and slower. As a result, despite different best-fit values, given the large uncertainties the estimated kinematics are roughly consistent with each other and even consistent with that of the filamentary screen found previously. It is possible that their variations are caused by the same scattering screen and the original filament is only part of a big structure, or their variations are from different origins.

One interesting thing we noticed is the clustered sky distribution of 22 variables, as shown in Fig. 10. The total survey sky coverage is  $1476 \, \mathrm{deg^2}$ , but 21 of 22 objects are discovered in three relatively small areas: seven are in the S190814bv field, within a  $\sim 10 \, \mathrm{deg^2}$  area (near the south Galactic pole); 11 are in the SB25077 and adjacent SB10636 fields, within a  $\sim 50 \, \mathrm{deg^2}$  area (galactic latitude *b* 

from  $-30^\circ$  to  $-40^\circ$ ); three are in the SB9434 and adjacent SB10635 fields, within a  $\sim 15 \ \text{deg}^2$  area (b from  $-48^\circ$  to  $-53^\circ$ ). The only remaining object is VAST J104933.6–245653 in the SB10612 field (around  $b=30^\circ$ ). This clustering is unusual, and at least implies that these regions have a greater abundance of turbulent gas clouds than other regions. Although we found no obvious association between these regions and H $\alpha$  intensity.

Redfield & Linsky (2008) identified 15 local ISM clouds and proposed interactions between their boundaries as the origin of enhanced radio-wave scintillation. We found the locations of our variables are near to some of cloud-cloud interaction boundaries. For example, the 11 variables identified in TESS field (Fig. 10) are extremely close to the boundaries of the 'G', 'Vel', 'Cet' clouds, and less favourably, the 'Blue', and 'Dor' clouds. Further observations are needed to establish the annual modulation of the scintillation rate to determine the velocity of the screens along with the characteristic scale. This can then be used to compare with proposed clouds kinematics.

Three clustered regions are about 75 deg<sup>2</sup> out of 1476 deg<sup>2</sup> total sky coverage, we therefore expect that 5 per cent of sky are active regions with a number of extreme scintillators. Note not all compact objects within the active regions are scintillating, and the fraction of actual plasma screens should be much less than 5 per cent. Using our searching technique, we expect to detect more extreme scintillators in future all-sky surveys (e.g. EMU and WALLABY). This would give us a systematic view of all-sky distribution of local plasma screens, allowing further inspection of association with cloud-cloud interaction boundaries and other scenarios.

#### 5.3 Variability rate analysis

We found 38 unique variable and transient sources in a sky area of  $1476 \, \text{deg}^2$  with total of 505 h observations. We analysed 52 8 – 10 h ASKAP fields and performed a variability search using 15-min model-subtracted snapshot images. Our variability search selected all sources detected in ~10 h model images and was therefore sensitive to any compact object with an averaged flux density of  $\gtrsim 0.18 \, \text{mJy}$  ( $5\sigma$  rms threshold). A two-epoch equivalent sky coverage (see Equation 1 in Bannister et al. 2011) of our survey is about  $88 \, 140 \, \text{deg}^2$ , which implies a variability rate of  $4.3 \times 10^{-4}$  sources per two-epoch deg<sup>2</sup>. If we exclude sources known to be Galactic (the stars and pulsars) this gives an surface density of  $2.5 \times 10^{-4}$  sources per two-epoch deg<sup>2</sup>. This value are consistent with predictions from Murphy et al. (2013) for commensal (EMU or WALLABY) surveys using snapshot images (see their Fig. 3).

For the overall  $1476 \, \mathrm{deg}^2$  sky area, the total number of unique sources is approximately  $7 \times 10^5$ . We found only a small fraction of sources (0.005 per cent) are variable – much lower than limit reported by previous searches (e.g. Mooley et al. 2016; Murphy et al. 2021). We note that variables or transient sources found in our survey (15-min time-scale) are considerably different from objects detected from previous radio transient survey (days to years time-scales; e.g. Bannister et al. 2011; Mooley et al. 2016). Our survey is more sensitive to pulsars, flaring radio stars, and enhanced scintillation of extragalactic objects, and not sensitive to extragalactic synchroton transients such as gamma-ray burst and tidal disruption events.

We calculated the detection sensitivity for flaring events with our survey strategy. We used the concept of fluence (unit of Jy s) in the calculation, defined as the product of the flaring time widths and the peak flux density values. As shown in Fig. 11, our 15-min snapshots survey are sensitive to transient events with a fluence limit of 1.1 Jy s when the characteristic time-scale is shorter than 15 min (e.g. for a

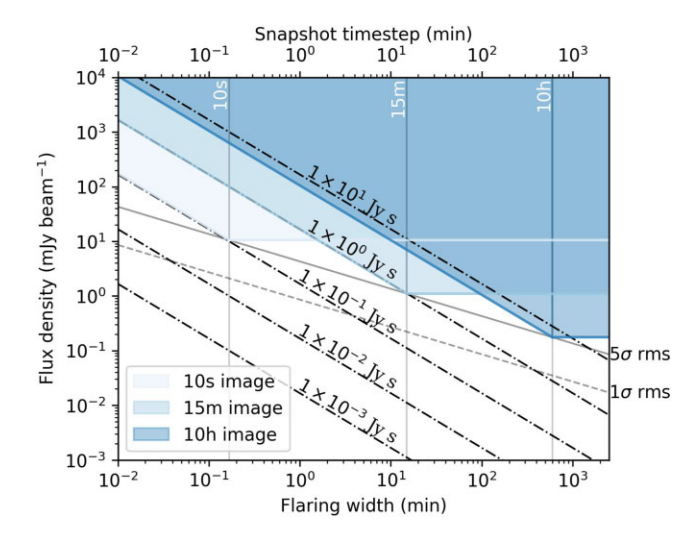


**Figure 11.** Transient source detection limit of the intra-observation survey strategy. The shallow area represents detectable transient events in different time-length (10 s, 15 min, and 10 h) snapshot images. The dotted-dashed lines represent the fluence of transient events. The grey dashed and solid line represent the  $1\sigma$  and  $5\sigma$  rms sensitivity for snapshot images in different time-lengths.

 $100\,\mathrm{Jy}$  burst with a duration of  $10\,\mathrm{ms}$ , or a  $8\,\mathrm{mJy}$  flare with a duration of  $2\,\mathrm{min}$ ), or with a peak flux density  $\gtrsim 1\,\mathrm{mJy}$  when the characteristic time-scale is longer than  $15\,\mathrm{min}$  and shorter than  $\sim 10\,\mathrm{h}$  (all are in  $5\sigma$  rms threshold). For a similar survey using 10-s snapshot images, we are more sensitive to shorter flares, for example, a fluence limit of  $0.18\,\mathrm{Jy}\,\mathrm{s}$  for an event with the time-scale shorter or comparable to  $10\,\mathrm{s}$ . On this time-scale we are able to detect fast radio burst-like events (e.g. Lorimer et al. 2007), or single pulses from ultra-long-period neutron stars (e.g. Caleb et al. 2022; Hurley-Walker et al. 2022b).

#### 5.4 Detection rate of stellar objects

We calculated the detection rate of stellar objects in our survey. We found total of eight stars in a  $1476\,\mathrm{deg^2}$  sky area, corresponding to a surface density of  $5.4\times10^{-3}\,\mathrm{deg^{-2}}$ . If we consider a 15-min snapshot equivalent sky coverage (i.e. treat each model-subtracted 15-min image as an independent sky-region snapshot image), we get a surface density of  $9.1\times10^{-5}\,\mathrm{deg^{-2}}$ . This rate is an order of magnitude lower than the surface density of  $9.66\times10^{-4}\,\mathrm{deg^{-2}}$  reported by Pritchard et al. (2021), who used 15-min ASKAP images at a similar observing frequency, with all-sky coverage. This could be due to multiple factors.

- (i) **Survey strategy**: Pritchard et al. (2021) conducted a circular polarization survey (finding any emission in 15-min stokes V images), whereas our survey focused on flux variations within a series of 15-min snapshot images. Our search is less sensitive to the quiescent, polarized emission produced by RS Canum Venaticorum stars, for example.
- (ii) **Independence of consecutive 15-min snapshots**: variable radio emission produced either due to rotational modulation of an active region of the stellar corona or stochastic flaring in localized coronal loops is unlikely to be independent on 15-min time-scales.
- (iii) **Small sampling of the duty cycle distribution**: a search for flaring objects in a deep observation only allows for detection of a small number of stars within the field of view. The majority of stars that are detectable by ASKAP have duty cycles well below 0.05

(Pritchard et al. 2023, in prep.), and therefore repeat sampling of the same field is more likely to sample a small group of low-duty cycle stars compared to a shallow, wide-field search that also covers the less common, highly active stars.

#### 5.5 Future plans

This work is a demonstration of functionality of our search technique. ASKAP began full survey operations in November 2022. We plan to run our transient detection pipeline commensally on other ASKAP observations, including two wide-field surveys: EMU/POSSUM $^{12}$  and WALLABY. Both of them will cover the entire Southern sky extending as far North as  $+30^{\circ}$  in declination, with  $8-10\,h$  integration time per pointing at 943.5 MHz or 1367.5 MHz. This will extend our work to an all-sky scale, enabling a comprehensive investigation for minute-time-scale transients.

Future improvements on our pipeline will focus on reducing processing time (An et al., in prep), which is now mainly limited by data transferring time and model generating ( $\sim 20\,h$ ). We also plan to implement our pipeline into the Pawsey Supercomputing Research Centre's Setonix supercomputer, where data transferring is not needed. The standard ASKAP processing for each survey will also be conducted in Setonix, and model images will be generated during this process. With these benefits the running time for our transient detection pipeline can be reduced down to a few minutes. This will enable rapid trigger and follow-up for individual transient events during full survey operation.

In this work we identified 11 transients and variables in the  $\sim 300 \, \text{deg}^2$  EMU pilot observations (i.e.  $\sim 1$  high variable per EMU field). Scaling to the ASKAP full survey, we are likely to identify  $\sim 1$  source per day assuming one 10-h ASKAP observation per day during full operation, or total of  $\sim 1000$  highly variable sources in the full EMU survey using the same technique.

We are able to explore different time-scales in future, for example, a 10-s snapshot survey would be able to detect fast radio burst-like events, or ultra-long-period neutron stars. Both of these object classes have not been fully understood yet. On this time-scale it would be possible to identify other unknown transient classes, expanding the understanding of radio time-domain phenomena.

# 6 CONCLUSIONS

We conducted the first radio transients survey to explore minute-time-scale variability within hours-long observations. We used ASKAP pilot survey data, consisting of 52 8 – 10 h observations at around 1 GHz, with a typical rms level of 30  $\mu$ Jy beam<sup>-1</sup>. The total sky coverage was 1476 deg<sup>2</sup> with overall observing time of 505 h.

We detected 38 transients and variable sources: 22 of them (59 per cent) are extreme scintillating objects caused by local plasma screens, eight (21 per cent) are stellar objects, seven (18 per cent) are pulsars, and the remaining one object (2 per cent) is an unidentified transient. We observed narrow-band scintles in the dynamic spectra for six (out of seven) pulsars, implying that diffractive scintillation is the main reason for pulsar variations on this time-scale. The remaining pulsar PSR J2039−5617 is a MSP in a binary system and the variability is due to eclipse. For stellar objects, their light curves have diverse morphologies ranging from short duration bursts (seconds—minutes) to long duration variations (≳hours). For 22 variables associated with AGN or galaxies, their variations are likely

<sup>&</sup>lt;sup>12</sup>POSSUM is commensal with EMU.

caused by local plasma screens. Their sky distribution is unusual: 21 are clustered in three small regions with an area of  $10-50\,\mathrm{deg^2}$  each (overall occupying 5 per cent fraction of our survey coverage). The reason for this clustering is unclear.

Future work on our searching pipeline will focus on the implementation into Setonix supercomputer, which would largely reduce the data processing time down to a few minutes. We will also incorporate better methods for dealing with correlated pixels and exploring different time-scales as well as detailed rates calculations. We expect to identify about 1000 transient and variable sources in the EMU full survey. The majority of these are likely to be extreme scintillating objects, which can help to establish an all-sky distribution of local plasma screens. We also expect to find  $\sim\!\!20$  unidentified objects which can possibly be new classes.

#### **ACKNOWLEDGEMENTS**

We would like to thank the referee for their helpful comments and suggestions. We thank Lister Staveley-Smith, Hayley Bignall, and Ron Ekers for useful discussions. YW is supported by the China Scholarship Council. Parts of this research were conducted by the Australian Research Council Centre of Excellence for Gravitational Wave Discovery (OzGrav), project number CE170100004.

This research was supported by the Sydney Informatics Hub (SIH), a core research facility at the University of Sydney. This work used resources of China SKA Regional Centre prototype (An et al. 2019; An et al. 2022) funded by National SKA Programme of China (2022SKA0130103) and the National Key R&D Programme of China (2018YFA0404603). This research has made use of the VizieR catalogue access tool, CDS, Strasbourg, France (DOI: 10.26093/cds/vizier). The original description of the VizieR service was published in Ochsenbein, Bauer & Marcout (2000). This research has made use of the SIMBAD data base, operated at CDS, Strasbourg, France (Wenger et al. 2000). This research has made use of data obtained from the *Chandra* Source Catalogue, provided by the *Chandra* X-ray Center (CXC) as part of the *Chandra* Data Archive.

This scientific work uses data obtained from Inyarrimanha Ilgari Bundara/the Murchison Radio-astronomy Observatory. We acknowledge the Wajarri Yamaji People as the Traditional Owners and native title holders of the Observatory site. CSIRO's ASKAP radio telescope is part of the Australia Telescope National Facility<sup>14</sup> Operation of ASKAP is funded by the Australian Government with support from the National Collaborative Research Infrastructure Strategy. ASKAP uses the resources of the Pawsey Supercomputing Research Centre. Establishment of ASKAP, Inyarrimanha Ilgari Bundara, the CSIRO Murchison Radio-astronomy Observatory and the Pawsey Supercomputing Research Centre are initiatives of the Australian Government, with support from the Government of Western Australia and the Science and Industry Endowment Fund. This paper includes archived data obtained through the CSIRO ASKAP Science Data Archive, CASDA (http://data.csiro.au).

This research has made use of APLPY (Robitaille & Bressert 2012), ASTROPY (Astropy Collaboration et al. 2013, 2018), ASTROQUERY (Ginsburg et al. 2019), MATPLOTLIB (Hunter 2007), MOCPY<sup>15</sup>, NUMPY (Harris et al. 2020), PYGSM (Price 2016), and SCIPY (Virtanen et al. 2020).

## 7 DATA AVAILABILITY

All of the ASKAP data used in this paper can be accessed through the CSIRO ASKAP Science Data Archive (CASDA<sup>13</sup>), using the project codes and SBIDs listed in Table 1.

#### REFERENCES

Abbott T. M. C., et al., 2018, ApJS, 239, 18

An T., Wu X.-P., Hong X., 2019, Nature Astronomy, 3, 1030

An T., Wu X., Lao B., Guo S., Xu Z., Lv W., Zhang Y., Zhang Z., 2022, Science China Physics, Mechanics, and Astronomy, 65, 129501

Astropy Collaboration et al., 2013, A&A, 558, 33

Astropy Collaboration et al., 2018, AJ, 156, 123

Backer D. C., 1970, Nature, 228, 42

Bailer-Jones C. A. L., Rybizki J., Fouesneau M., Demleitner M., Andrae R., 2021, AJ, 161, 147

Bannister K. W., Murphy T., Gaensler B. M., Hunstead R. W., Chatterjee S., 2011, MNRAS, 412, 634

Becker R. H., White R. L., Helfand D. J., 1995, ApJ, 450, L559

Beers T. C., Rossi S., Ulrich D., Wilhelm R., 1996, AJ, 112, 1188

Bell M. E., et al., 2011, MNRAS, 415, 2

Bell M. E., et al., 2019, MNRAS, 482, 2484

Bhat N. D. R., Gupta Y., Rao A. P., 1998, ApJ, 500, L262

Bhattacharyya B., et al., 2016, ApJ, 817, L130

Bhattacharyya B., et al., 2019, ApJ, 881, L59

Bignall H., et al., 2019, MNRAS, 487, 4372

Bower G. C., Saul D., Bloom J. S., Bolatto A., Filippenko A. V., Foley R. J., Perley D., 2007, ApJ, 666, L346

Briggs D. S., 1995, PhD thesis, New Mexico Institute of Mining and Technology

Caleb M., et al., 2022, Nature Astronomy, 6, 828

Camilo F., Lorimer D. R., Freire P., Lyne A. G., Manchester R. N., 2000, ApJ, 535, L975

Chen K., Ruderman M., 1993, ApJ, 402, L264

Chiti A., Chatterjee S., Wharton R., Cordes J., Lazio T. J. W., Kaplan D. L., Bower G. C., Croft S., 2016, ApJ, 833, L11

Clark C. J., et al., 2021, MNRAS, 502, 915

Cordes J. M., 1986, ApJ, 311, L183

Cordes J. M., Lazio T. J. W., 2002, preprint (astro-ph/0207156)

Cordes J. M., Lazio T. J. W., McLaughlin M. A., 2004, New A Rev., 48, 1459

Corongiu A., et al., 2021, MNRAS, 502, 935

Das B., et al., 2022, ApJ, 925, 125

DeBoer D. R., et al., 2009, IEEE Proceedings, 97, 1507

Dennett-Thorpe J., de Bruyn A. G., 2002, Nature, 415, 57

Dennett-Thorpe J., de Bruyn A. G., 2003, A&A, 404, 113

Dey A., et al., 2019, AJ, 157, 168

Dobie D., et al., 2019, ApJ, 887, L13

Dobie D., et al., 2022, MNRAS, 510, 3794

Dulk G. A., 1985, ARA&A, 23, 169

Duncan K. J., 2022, MNRAS, 512, 3662

Evans I. N., et al., 2010, ApJS, 189, 37

Fender R., et al., 2016, in MeerKAT Science: On the Pathway to the SKA. Stellenbosch, South Africa, p. 13

Finch C. T., Zacharias N., Subasavage J. P., Henry T. J., Riedel A. R., 2014, AJ, 148, 119

Flesch E. W., 2015, PASA, 32, e010

Flesch E. W., 2021, preprint (arXiv:2105.12985)

Fouqué P., et al., 2018, MNRAS, 475, 1960

Freund S., Robrade J., Schneider P. C., Schmitt J. H. M. M., 2018, A&A, 614, 125

Freund S., Czesla S., Robrade J., Schneider P. C., Schmitt J. H. M. M., 2022, A&A, 664, 105

Gaensler B. M., Landecker T. L., Taylor A. R., POSSUM Collaboration, 2010, in American Astronomical Society Meeting Abstracts #215. p. 470.13

<sup>14</sup>https://ror.org/05qajvd42

<sup>&</sup>lt;sup>15</sup>https://github.com/cds-astro/mocpy

<sup>13</sup>https://data.csiro.au/dap/public/casda/casdaSearch.zul

```
Gaia Collaboration et al., 2016, A&A, 595, 1
                                                                               Murphy T., et al., 2021, PASA, 38, e054
Gaia Collaboration et al., 2018, A&A, 616, 1
                                                                               Narayan R., 1992, Philosophical Transactions of the Royal Society of London
Gaia Collaboration, et al., 2022, preprint (arXiv:2208.00211)
                                                                                   Series A, 341, 151
Gal-Yam A., et al., 2006, ApJ, 639, L331
                                                                               Newton L. M., Manchester R. N., Cooke D. J., 1981, MNRAS, 194, 841
Ginsburg A., et al., 2019, AJ, 157, 98
                                                                               Norris R. P., et al., 2011, PASA, 28, 215
                                                                               Norris R. P., et al., 2021, PASA, 38, e046
Güdel M., 2002, ARA&A, 40, 217
Günther M. N., et al., 2020, AJ, 159, 60
                                                                               Obenberger K. S., et al., 2014, ApJ, 785, L27
Guzman J., et al., 2019, ASKAPsoft: ASKAP science data processor software,
                                                                               Ochsenbein F., Bauer P., Marcout J., 2000, A&AS, 143, 23
   Astrophysics Source Code Library, record ascl:1912.003
                                                                               Oosterloo T. A., et al., 2020, A&A, 641, 4
                                                                               Osten R. A., 2008, preprint (arXiv:0801.2573)
Haakonsen C. B., Rutledge R. E., 2009, ApJS, 184, 138
                                                                               Philippov A., Kramer M., 2022, ARA&A, 60, 495
Hale C. L., et al., 2021, PASA, 38, e058
                                                                               Prasad P., et al., 2016, Journal of Astronomical Instrumentation, 05, 1641008
Hancock P. J., Murphy T., Gaensler B. M., Hopkins A., Curran J. R., 2012,
                                                                               Price D. C., 2016, PyGSM: Python interface to the Global Sky Model,
   MNRAS, 422, 1812
Hancock P. J., Trott C. M., Hurley-Walker N., 2018, PASA, 35, e011
                                                                                   Astrophysics Source Code Library, record ascl:1603.013
                                                                               Pritchard J., et al., 2021, MNRAS, 502, 5438
Harris C. R., et al., 2020, Nature, 585, 357
                                                                               Rau U., Cornwell T. J., 2011, A&A, 532, 71
Hobbs G., et al., 2016, MNRAS, 456, 3948
                                                                               Redfield S., Linsky J. L., 2008, ApJ, 673, L283
Hotan A. W., et al., 2021, PASA, 38, e009
                                                                               Riaz B., Gizis J. E., Harvin J., 2006, AJ, 132, 866
Houdebine É. R., Mullan D. J., Doyle J. G., de La Vieuville G., Butler C. J.,
                                                                               Ricker G. R., et al., 2015, Journal of Astronomical Telescopes, Instruments,
   Paletou F., 2019, AJ, 158, 56
Hovatta T., Valtaoja E., Tornikoski M., Lähteenmäki A., 2009, A&A, 494,
                                                                                   and Systems, 1, 014003
                                                                               Rigney J., et al., 2022, MNRAS, 516, 540
   527
                                                                               Rimmer W. B., 1930, Memoires of the Mount Stromlo Observervatory, 2, 1
Hunter J. D., 2007, Computing in Science and Engineering, 9, 90
Hurley-Walker N., et al., 2017, MNRAS, 464, 1146
                                                                               Robitaille T., Bressert E., 2012, APLpy: Astronomical Plotting Library in
Hurley-Walker N., et al., 2022a, PASA, 39, e035
                                                                                   Python, Astrophysics Source Code Library, record ascl:1208.017
Hurley-Walker N., et al., 2022b, Nature, 601, 526
                                                                               Rowlinson A., et al., 2019, Astronomy and Computing, 27, 111
Hyman S. D., Lazio T. J. W., Kassim N. E., Ray P. S., Markwardt C. B.,
                                                                               Sebastian D., et al., 2021, A&A, 645, 100
                                                                               Shimwell T. W., et al., 2017, A&A, 598, 104
   Yusef-Zadeh F., 2005, Nature, 434, 50
                                                                               Skrutskie M. F., et al., 2006, AJ, 131, 1163
Intema H. T., Jagannathan P., Mooley K. P., Frail D. A., 2017, A&A, 598, 78
                                                                               Sobey C., et al., 2022, A&A, 661, 87
Jeffries R. D., Bromage G. E., 1993, MNRAS, 260, 132
                                                                               Stewart A. J., et al., 2016, MNRAS, 456, 2321
Jerzykiewicz M., Sterken C., 1993, MNRAS, 260, 826
Johnson H. L., Mitchell R. I., 1975, RMxAA, 1, 299
                                                                               Taylor J. H., Manchester R. N., Lyne A. G., 1993, ApJS, 88, 529
                                                                               Thyagarajan N., Helfand D. J., White R. L., Becker R. H., 2011, ApJ, 742,
Kaplan D. L., et al., 2019, ApJ, 884, L96
                                                                                  L49
Kedziora-Chudczer L., Jauncey D. L., Wieringa M. H., Walker M. A.,
   Nicolson G. D., Reynolds J. E., Tzioumis A. K., 1997, ApJ, 490, L9
                                                                               Traulsen I., et al., 2020, A&A, 641, 137
                                                                               Trigilio C., Leto P., Leone F., Umana G., Buemi C., 2000, A&A, 362, 281
Kellermann K. I., Pauliny-Toth I. I. K., 1969, ApJ, 155, L71
                                                                               Villadsen J., Hallinan G., 2019, ApJ, 871, L214
Koribalski B. S., et al., 2020, Ap&SS, 365, 118
                                                                               Virtanen P., et al., 2020, Nat. Methods, 17, 261
Lacy M., et al., 2020, PASP, 132, 035001
                                                                               Voges W., et al., 1999, A&A, 349, 389
Lazio T. J. W., et al., 2010, AJ, 140, 1995
                                                                                Walker M. A., 1998, MNRAS, 294, 307
Lee J., Song I., Murphy S. J., 2022, MNRAS, 511, 6179
                                                                               Walker M. A., Tuntsov A. V., Bignall H., Reynolds C., Bannister K. W.,
Leto P., et al., 2020, MNRAS, 493, 4657
                                                                                   Johnston S., Stevens J., Ravi V., 2017, ApJ, 843, L15
Levinson A., Ofek E. O., Waxman E., Gal-Yam A., 2002, ApJ, 576, L923
                                                                               Wang Y., Tuntsov A., Murphy T., Lenc E., Walker M., Bannister K., Kaplan
Lorimer D. R., Kramer M., 2012, Handbook of Pulsar Astronomy. Cambridge
                                                                                  D. L., Mahony E. K., 2021, MNRAS, 502, 3294
   University Press, Cambridge, UK
                                                                               Wang Y., et al., 2022, ApJ, 930, L38
Lorimer D. R., Bailes M., McLaughlin M. A., Narkevic D. J., Crawford F.,
   2007, Science, 318, 777
                                                                               Watson C. L., Henden A. A., Price A., 2006, Society for Astronomical
Malo L., Artigau É., Doyon R., Lafrenière D., Albert L., Gagné J., 2014, ApJ,
                                                                                   Sciences Annual Symposium, 25, 47
                                                                               Wegner G., 1981, AJ, 86, 264
   788, L81
Manchester R. N., Hobbs G. B., Teoh A., Hobbs M., 2005, AJ, 129, 1993
                                                                               Wenger M., et al., 2000, A&AS, 143, 9
                                                                               Whiting M. T., 2020, in Ballester P., Ibsen J., Solar M., Shortridge K.eds,
Mauch T., Murphy T., Buttery H. J., Curran J., Hunstead R. W., Piestrzynski
                                                                                   Astronomical Society of the Pacific Conference Series Vol. 522, Astro-
   B., Robertson J. G., Sadler E. M., 2003, MNRAS, 342, 1117
                                                                                   nomical Data Analysis Software and Systems XXVII. p. 469
McConnell D., et al., 2020, PASA, 37, e048
McMullin J. P., Waters B., Schiebel D., Young W., Golap K., 2007, in Shaw R.
                                                                               Whiting M., Humphreys B., 2012, PASA, 29, 371
                                                                               Wright E. L., et al., 2010, AJ, 140, 1868
   A., Hill F., Bell D. J.eds, Astronomical Society of the Pacific Conference
                                                                               Wu Z., et al., 2022, A&A, 663, 116
   Series Vol. 376, Astronomical Data Analysis Software and Systems XVI.
                                                                               Zheng H., et al., 2017, MNRAS, 464, 3486
                                                                               Zic A., et al., 2020, ApJ, 905, L23
Moe M., Di Stefano R., 2015, ApJ, 801, L113
Moe M., Di Stefano R., 2017, ApJS, 230, 15
```

This paper has been typeset from a  $T_EX/IAT_EX$  file prepared by the author.

Mooley K. P., et al., 2016, ApJ, 818, 105 Murphy T., et al., 2013, PASA, 30, e006

Murphy S. J., Lawson W. A., Bento J., 2015, MNRAS, 453, 2220